

ADA058009

AD No. \_\_\_\_\_  
DDC FILE COPY

LEVEL #

12

ARPA ORDER NO. 3363

INTERIM TECHNICAL REPORT  
DEVELOPMENT OF A TABLE TOP MODEL FOR THE GENERATION  
OF AMORPHOUS/MICROCRYSTALLINE METAL POWDERS

OFFICE OF NAVAL RESEARCH  
CONTRACT NO. N00014-77-C-0373  
01 MAY 1977 - 30 APRIL 1978

Principal Investigator:

John F. Mahoney  
(213) 357-3201

DDC  
RECEIVED  
AUG 23 1978  
A

$\Phi$  PHRASOR TECHNOLOGY

1536 Highland Avenue  
Duarte, California 91010

DISTRIBUTION STATEMENT A  
Approved for public release;  
Distribution Unlimited

The views and conclusions contained in this report are those of Phrasor Technology and should not be interpreted as necessarily representing the official policies, either express or implied, of the Defense Advanced Research Projects Agency, or the United States Government.

78 08 14 071

ERRATA SHEET  
FOR  
INTERIM TECHNICAL REPORT  
DEVELOPMENT OF A TABLE TOP MODEL FOR THE GENERATION  
OF AMORPHOUS/MICROCRYSTALLINE METAL POWDERS  
Phrasor Technology  
Report Number 78-1  
June 1978

Listed below are the corrections to be made in this  
Interim Technical Report:

(Front Cover) second line from bottom. The word "express"  
should read "expressed"

SECTION 2 APPLICATION . . - page 2-1,

--line 14. The word "solidifcation" is misspelled  
and should read, --solidification--

--page 2-3, TABLE I heading, first word, "LIQUIDIS" is  
misspelled and should read, --LIQUIDUS--

--page 4-7, 3rd para., --line 14 - delete the parentheses  
")" before word, "yielding"

5.2 RADIATION COOLING - page 5-4

--line 5, the word "hemipshercial" is misspelled and  
should read, --hemispherical--

--page 6-9, 2nd para., the word "underway" should be  
written as two words, --under way--

--page 6-10, 2nd para., 3rd line from bottom of page,  
the word "underway" should be two words, --under way--

SECTION 7 CONCLUSIONS b. 2nd line. Delete figures "5.4"  
and insert --4.5--. It should read, --Al-4.5% Cu alloy--

REFERENCES - 11. Last name "Vickets" is misspelled and  
should read, --K. E. Vickers--

UNCLASSIFIED

SECURITY CLASSIFICATION OF THIS PAGE (When Data Entered)

REPORT DOCUMENTATION PAGE		READ INSTRUCTIONS BEFORE COMPLETING FORM
1. REPORT NUMBER 141/78-1	2. GOVT ACCESSION NO.	3. RECIPIENT'S CATALOG NUMBER
4. TITLE (and Subtitle) DEVELOPMENT OF A TABLE TOP MODEL FOR THE GENERATION OF AMORPHOUS/MICROCRYSTALLINE METAL POWDERS		5. TYPE OF REPORT & PERIOD COVERED Interim Technical report 01 May 1977 - 30 Apr 1978
6. AUTHOR(s) John F. Mahoney, Kenneth E. Vickers Bernard E. Kalensher, Julius Perel		7. PERFORMING ORG. REPORT NUMBER
8. PERFORMING ORGANIZATION NAME AND ADDRESS Phrasor Technology 1536 Highland Avenue Duarte, California 91010		9. CONTRACT OR GRANT NUMBER(s) N00014-77-C-0373 WARPA Order-3363
10. CONTROLLING OFFICE NAME AND ADDRESS Procuring Contracting Officer Office of Naval Research/Dept. of the Navy 800 Quincy St., Arlington, Virginia 22217		11. PROGRAM ELEMENT, PROJECT, TASK AREA & WORK UNIT NUMBERS 12/72p
11. MONITORING AGENCY NAME & ADDRESS (if different from Controlling Office) Defense Contracts Administration Services 3452 East Foothill Blvd. Pasadena, California 91107		12. REPORT DATE Jun 1978
12. DISTRIBUTION STATEMENT (of this Report) Reproduction of this report in whole or in part is permitted for any purpose of the United States Government.		13. NUMBER OF PAGES 67
13. DISTRIBUTION STATEMENT (of the abstract entered in Block 20, if different from Report)		14. SECURITY CLASS. (of this report) Unclassified
14. SUPPLEMENTARY NOTES		15a. DECLASSIFICATION/DOWNGRADING SCHEDULE
15. KEY WORDS (Continue on reverse side if necessary and identify by block number) Electrohydrodynamics      Microcrystals Amorphous Alloys      Powder Metallurgy Deposition      Microspheres Rapid Solidification		
16. ABSTRACT (Continue on reverse side if necessary and identify by block number) The electrohydrodynamic (EHD) technique for the generation of liquid droplets was employed to produce micron size metal powders. This was accomplished using a laboratory feasibility model apparatus which was developed on the program. The aim of the program is the development of a table top powder generator cap- able of controlled production of ultrafine powders at high cooling rates. The table top generator is to be used in the fundamental studies of the effect of solidification variables on microstructures and the development of new alloy compositions. New ceramic EHD sources were developed capable of operating up		

cont  
L→

UNCLASSIFIED

SECURITY CLASSIFICATION OF THIS PAGE(When Data Entered)

to 1400°C with promise of little or no corrosion. Particles below 0.1 to 100 micron were generated with cooling rates extending up to  $10^6$  °K/second. Coatings a few microns thick were made on metal substrates with no layering effects observed in the coatings. In addition, evidence of welding between a splat foil and the metal substrate was seen. Analytical studies indicate that equations defining the cooling of submicron particles can not be obtained from simple extrapolation of macroscopic heat transfer theory.

X

1,000,000 K/second.

14730

UNCLASSIFIED

SECURITY CLASSIFICATION OF THIS PAGE(When Data Entered)

## FOREWORD

The information presented in this report was generated under ARPA Order Number 3363 and ONR Contract Number N00014-77-C-0373. The work was performed by Phrasor Technology, Duarte, California.

This program was initiated under the direction of Dr. Edward C. Van Reuth, Materials Science, Defense Advanced Research Projects Agency, and the Scientific Officer is Dr. Bruce A. MacDonald, Materials Science Division, Office of Naval Research, Arlington, Virginia. The work was performed from 1 May 1977 to 30 April 1978.

The principal investigator for the program was Mr. John F. Mahoney (213) 357-3201 of Phrasor Technology, 1536 Highland Avenue, Duarte, California 91010. Work on the program was also performed by Dr. Bernard E. Kalensher, Dr. Julius Perel, and Mr. J. Robert Otto. In addition, consultation assistance was obtained from Professor Pol Duwez, Professor Robert Mehrabian, and Mr. Hoyt Todd.

The views and conclusions contained in this document are those of Phrasor Technology and should not be interpreted as necessarily representing the official policies, either expressed or implied, of the Defense Advanced Research Projects Agency or the United States Government.

**ADDITION FOR**

WTS	Other Surveys	<input checked="" type="checkbox"/>
EEO	Rent Survey	<input type="checkbox"/>
UNEMPLOYED		<input type="checkbox"/>
JUSTIFICATION.....		

BY.....

DIVISION/STATION/UNIT NAME

DATE TIME OF SPECIAL

A

78 08 14 071

## CONTENTS

1.	INTRODUCTION AND SUMMARY	1-1
2.	APPLICATION TO FUNDAMENTAL STUDIES IN RAPID SOLIDIFICATION	2-1
2.1	Amorphous Structures	2-2
2.2	Crystalline Structures	2-4
3.	EXPERIMENTAL APPROACH	3-1
3.1	Review of Electrohydrodynamics	3-1
3.2	Experimental Apparatus, The Feasibility Model	3-5
4.	DEVELOPMENT OF THE EHD SOURCE FOR THE FEASIBILITY MODEL	4-1
4.1	Materials Considerations	4-1
4.2	Thermal Considerations	4-4
4.3	Flow Control	4-6
5.	HEAT FLOW DURING SOLIDIFICATION OF THE MICRODROPLETS	5-1
5.1	Power Loss and Solidification Time	5-1
5.2	Radiation Cooling	5-4
5.3	Convective Cooling	5-6
5.4	Calculation of Solidification Time and Cooling Rate	5-7
5.5	Heating of Microparticles on Impact	5-13
6.	EXPERIMENTAL RESULTS	6-1
6.1	Atomization Studies	6-2
6.2	Splat Cooling Studies	6-9
7.	CONCLUSIONS	7-1
	REFERENCES	R-1

PRECEDING PAGE NOT FILMED  
BLANK

## ILLUSTRATIONS

1	Microstructure of Undercooled Ni-30% Cu Alloy Specimens	2-7
2	Electrohydrodynamic Generation of Charged Droplets	3-2
3	Electrohydrodynamic Droplet Generator	3-4
4	Feasibility Model Source Operations Diagram	3-6
5	Feasibility Model	3-7
6	Electrical Schematic for Microparticle Source Operation	3-10
7	Schematic Diagram of the Horizontal Source in the Feasibility Model	4-2
8	Photographs of the All-Ceramic (mullite) Source in the Feasibility Model	4-5
9	Solidification Time versus Droplet Radius, for Radiative Cooling	5-9
10	Cooling Rate versus Droplet Radius, for Radiative Cooling	5-11
11	Distance Traveled by Droplets During Solidification versus Droplet Radius, for Radiative Cooling	5-14
12	Conditions on Particle Heating Upon Impact	5-17
13	Secondary Electron Images of Fine Atomized Powders of Al-4.5% Cu Alloy Produced by the EHD Technique	6-3
14	Secondary Electron Image of Fine Atomized Powders of Al-4.5% Cu Alloy Produced by the EHD Technique	6-4
15	Scanning Electron Images of Coarse Atomized, 100 to 150 $\mu$ m, Powders of Al-4.5% Cu Alloy Produced in the EHD Apparatus	6-6
16	Scanning Electron Images of an Al-4.5% Cu Coarse Powder Almost Completely Solidified Before Impact	6-7
17	Back Scattered Electron Images of the Internal Dendritic Structure of a Coarse Powder of Al-4.5% Cu Alloy Produced by the EHD Technique	6-8
18	Secondary Electron Images of a Splat Cooled Specimen of Al-4.5% Cu Alloy Produced in the EHD Apparatus on a Copper Substrate	6-11

ILLUSTRATIONS (contd)

- |    |  |      |
|----|--|------|
| 19 | Secondary Electron Images of a Splat Cooled Specimen of Al-4.5% Cu Alloy Produced in the EHD Apparatus on an Aluminum Substrate                  | 6-12 |
| 20 | Secondary Electron Images of a Splat Cooled Specimen of Al-4.5% Cu Alloy Produced in the EHD Apparatus on a Vinyl Cellulose Substrate            | 6-14 |
| 21 | Cross Sectional View of an Al-4.5% Cu Alloy Splat Cooled Specimen Deposited on an Aluminum Substrate Showing Evidence of Welding Between the Two | 6-15 |

## SECTION 1

### INTRODUCTION AND SUMMARY

The advent of a new understanding of materials derived from rapid solidification and supercooling has led to the need for new laboratory devices for the researchers. The researcher desires a means of making various small samples of specific alloys that can be cooled at rates of  $10^2$  to  $10^{10}$  degrees per second. The investigation of a wide variety of alloys under varying rates of cooling could enhance the understanding of the fundamental properties and physical phenomena associated with amorphous or microcrystalline structures. The Department of Defense Advanced Research Projects Agency through the Materials Sciences initiated this program to evolve a laboratory research tool; a tabletop system that could produce a wide variety of alloys at cooling rates exceeding  $10^8$  degrees per second. The system must be uncomplicated, versatile, reliable, and within the normal costs of research support equipment.

The technical approach pursued on this program for the development of a rapid solidification system was through the generation of molten metal particles by electrohydrodynamics (EHD). From an alloy melt, ultrafine charged particles can be generated, accelerated, and collected in a controlled manner. These ultrafine spheres can be cooled by means of radiative, convective, and conductive heat transfer. The size of particles, their velocity, and trajectory can be controlled in the EHD system. The program has as its main objective the development of the tabletop system with secondary objectives being the investigation of EHD for other materials processing applications such as thin film deposition, composition, implantation, etc.

The program that will develop the system has been divided into five main tasks, as follows:

- I. EHD Process Analysis
- II. Materials Investigation
- III. Laboratory Feasibility Model
- IV. Engineering Model
- V. Prototype Model

An analysis of the EHD process identified the influencing parameters of rapid solidification by the ultrafine particles produced. The materials investigation will select the most optimal materials for experimentation. The Laboratory Feasibility Model (LFM) was developed for variable parameter testing of the EHD process. The LFM design and experimental operation indicate that the EHD process does meet the technical requirements. Droplets were generated from below 0.1 micrometers to 100 micrometers. The cooling rates ranged from  $10^2$  to  $10^6$  degrees/second.

The program methodology planned is to use the experimental data to guide the design of the Engineering Model. This development model permits the testing and evaluation of components for inclusion in the final prototype design of the tabletop system.

This report covers the effort accomplished under the first three tasks, and preliminary consideration for task IV, the Engineering Model.

Significant results accomplished under the program were:

- a. Cooling rates of  $10^6$  degrees/second
- b. Particle size generation from below 0.1 to 100 micrometers
- c. Single crystal particle generation
- d. Impregnation of the droplets into substrate (welding)
- e. Thin films of  $6 \times 10^{-6}$  meters deposited with no structure or laminates apparent at 10,000 times magnification

The successful completion of this portion of the program has provided the confidence necessary to continue the development of the tabletop system.

## SECTION 2

### APPLICATION TO FUNDAMENTAL STUDIES IN RAPID SOLIDIFICATION

Fundamental and applied studies in rapid solidification processing have led to a new vista in possible useful material structures and compositions. Yet, our current understanding of the important interrelationships between process variables, e.g., alloy composition and cooling rate, and structure and microchemistry is in a relatively embryonic stage. The realization of the long range potential applications of rapid solidification processing requires a much better fundamental understanding of these phenomena through controlled, reproducible, scientific experiments coupled with theoretical considerations. The electrohydrodynamic apparatus under development in this investigation is aimed at providing the necessary laboratory tool for such investigations. It would permit the generation of a large range of fine, controlled size, atomized particles of a variety of low and high temperature alloys and their subsequent solidification in flight or on a variety of cold substrates.

A review of the available literature in the field of rapid solidification shows that the structures obtained in various alloy systems can be divided into two general categories; alloys that yield noncrystalline (amorphous) structures, and alloys that, under the present limitations of achievable cooling rates, form crystalline structures that exhibit:

- Metastable phases
- Increased solid solubility of solute elements
- Altered microsegregation patterns due to large undercoolings prior to nucleation

The following paragraphs contain a short review of some of the reported information on amorphous and crystalline structures noted above, and discuss its relevance to the subject of the present investigation.

## 2.1 AMORPHOUS STRUCTURES

It is generally agreed that alloy composition and cooling rate, prior to solidification, are the most important variables affecting formation of noncrystalline structures. Melt viscosity,  $\eta$ , and glass transition temperature,  $T_g$ , are two factors in glass formation that depend on alloy composition. Since the viscosity of most metallic melts near their melting point is of the order of a few centipoise, theoretical treatments of critical cooling rates,  $R_c$ , necessary for the formation of noncrystalline structures have been principally based on the magnitude of the reduced glass transition temperature,  $T_{rg} = T_g/T_m$ , where  $T_g$  corresponds to a melt viscosity of  $\eta \approx 10^{13}$  poise.

Davis and his coworkers (Ref. 1-3) have calculated the critical cooling rates,  $R_c$ , for the formation of amorphous structures in a number of alloys using a kinetic model based on theories of homogeneous nucleation, crystal growth, and transformation kinetics. A shortcoming of these calculations is that they are based on an assumed model of variation of viscosity,  $\eta$ , between the melting point of the alloy, and glass transition temperature,  $T_g$ . Nevertheless, predicted values of critical cooling rates,  $R_c$ , for a number of alloys close to eutectic compositions (high values of  $T_{rg}$ ) have been verified by experiment (Ref. 3). Table I lists the calculated values for a selected number of glass forming alloys.

The electrohydrodynamic apparatus developed in this investigation is most suitable for fundamental studies on alloys such as those listed in Table I. The controlled size fine droplets generated at the source can be solidified either in flight or on cold substrates. For example,

theoretical considerations presented in the following section show that at least in the radiative cooling regime a predictive mathematical model for heat flow is available which indicates that a large range of cooling rates during solidification are achievable as a function of droplet size.

TABLE I

LIQUIDUS TEMPERATURE,  $T_m$ , GLASS TRANSITION TEMPERATURE,  $T_g$ , AND CALCULATED CRITICAL COOLING RATES,  $R_c$ , FOR A NUMBER OF GLASS FORMING ALLOYS (from Ref. 3 and 4)

<u>Alloy Composition</u>	<u><math>T_m</math> (<math>^{\circ}</math>K)</u>	<u><math>T_g</math> (<math>^{\circ}</math>K)</u>	<u><math>T_{rg} = T_g/T_m</math></u>	<u><math>R_c</math> (<math>^{\circ}</math>K/sec)</u>
Pd <sub>77.5</sub> Cu <sub>6</sub> Si <sub>16.5</sub>	1015	653	0.64	$2 \times 10^2$
Pd <sub>82</sub> Si <sub>18</sub>	1071	657	0.61	$5 \times 10^3$
Ni <sub>62.4</sub> Nb <sub>37.6</sub>	1442	945	0.66	$2 \times 10^3$
Pd <sub>40</sub> Ni <sub>40</sub> P <sub>20</sub>	916	602	0.66	$1 \times 10^3$
Cu <sub>60</sub> Zr <sub>40</sub>	$\sim 1173$	673	0.57	$5 \times 10^3$
Fe <sub>80</sub> P <sub>13</sub> C <sub>7</sub>	1258	736	0.59	$5 \times 10^4$
Pt <sub>60</sub> Ni <sub>15</sub> P <sub>25</sub>	875	500	0.57	$8 \times 10^4$
Fe <sub>41.5</sub> Ni <sub>41.5</sub> B <sub>17</sub>	1352	720	0.53	$\sim 10^6$
METGLAS	1275	$\approx 500$ to 700	-	$\sim 10^4$

In the next phase of this investigation, a number of alloys representing a range of melting temperatures and critical cooling rates would be selected from Table I and used in experiments in the EHD apparatus. The aim of these experiments would be to further verify the capability

of the apparatus and to correlate the size of the fine powders and their cooling rates during solidification with analytical models of particle generation and heat flow developed in this program.

## 2.2 CRYSTALLINE STRUCTURES

The important influence of rapid cooling rates during crystalline solidification on the fineness of segregate spacings and the size and distribution of second phases has long been recognized. More recently, a number of fundamental investigations have shown that rapid solidification may also cause substantial cooling prior to nucleation of the solid (Ref. 4-7), increase the solid solubility of solute elements in the base metal (Ref. 8, 9), and result in the formation of metastable crystalline phases (Ref. 8, 9). Concurrent applied studies are presently underway to exploit the beneficial effects of this new technology in the production of complex alloy, fully dense, heat treatable parts (Ref. 9). It is anticipated that a major contribution of the EHD technique would be to permit rapid solidification of a variety of alloy compositions under controlled conditions with reproducible cooling rates. It should thus become an invaluable tool for fundamental studies aimed at enhancing our current limited understanding of rapid solidification and segregation phenomena, as well as the development of specific alloy compositions for future applications in innovative rapid solidification technologies.

Whether actual cooling rate during rapid crystalline solidification can be deduced from subsequent structural examination is now open to controversy (Ref. 4). It is generally agreed that average cooling rate during solidification can be deduced from measured dendrite arm spacings if:

- a. The rapidly solidified structure has a well defined (characteristic) dendrite structure
- b. The relationship between dendrite arm spacings and average cooling rate is already known for the specific alloy of interest over a large range of cooling rates

The fineness of microstructure during dendritic solidification is related to local solidification time,  $\tau$ . The dendrite arm spacing,  $d$ , and average cooling rate during solidification are given by:

$$d = a\epsilon_{\text{Avg}}^{-n} = b\tau^n \quad (1)$$

$$\epsilon_{\text{Avg}} = \frac{\Delta T}{\tau} \quad (2)$$

where  $\Delta T$  is solidification temperature range, and  $a$ ,  $b$ , and  $n$  are constants.

The constants in Eq. (1), over a large range of average cooling rates, have only been determined for a very few alloy systems. The most studied of this is Al-4.5% Cu. Equation (1) for this alloy over more than nine orders of magnitude in average cooling rate has been determined to be:

$$d = 40\epsilon_{\text{Avg}}^{-0.39} \quad (3)$$

The Al-4.5% Cu alloy was extensively used in the present program as a model system to study the range of particle sizes and cooling rates achievable in the EHD apparatus. Work to date, which is described in a later section, has shown that fine powders ranging in size from below 0.1 micrometer to over one hundred microns, as well as controlled thickness splats on various substrates, can be successfully produced by the EHD techniques.

Extension of solid solubility of solute elements, as well as formation of metastable phases, have been reported in rapidly solidified structures of a large number of alloys (Ref. 8). For example, lattice spacings measured by x-ray diffraction have shown increased solubility of copper, iron, silicon, nickel, and vanadium in aluminum with increasing cooling rate. From these data, one could correlate the calculated or measured cooling rate in a given rapid solidification process to the maximum reported solid solubility of an element. Similar studies on rapidly solidified aluminum alloys produced in the EHD apparatus are planned in the next phase of the program to establish the relationships between the specific variables of the process, the quenching techniques available, cooling rates achieved, and structure.

Significant undercooling prior to crystalline solidification affects both solute distribution and the morphology of the dendrites in the resulting structures. Solute-rich dendritic cores, which can be correlated to undercooling before nucleation, have been reported in a variety of alloy systems (Ref. 10, 5-7). For example, it has been established that a certain percentage of vacuum or inert gas atomized droplets of maraging 300 steel undercooled substantially before nucleation (Ref. 7).

As noted above, undercooling also affects the morphology of the dendrites which, in turn, would exclude direct correlation of dendrite arm spacings with cooling rates. Work on a variety of iron and nickel base alloys has shown that, at low undercoolings, 60 to 170°K, the usual fernlike dendritic structure reverts to one with cylindrical arms. Beyond a critical undercooling, 170°K, the dendritic structure changes into a spherical growth morphology. This change also manifests itself by a sudden decrease in grain size of the resulting solid. Figure 1 shows the changes in the microstructure of Ni-30% Cu alloy as a function of undercooling.

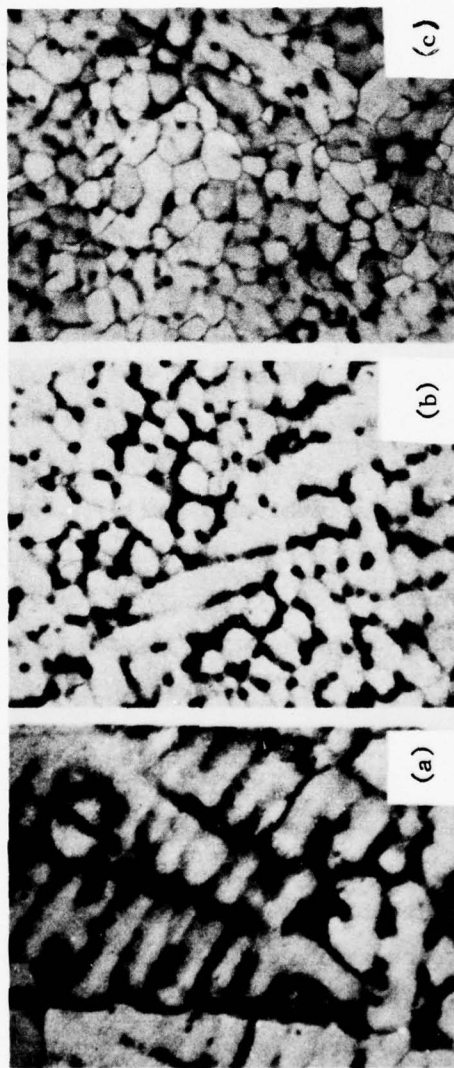


Figure 1. Microstructure of Undercooled Ni-30% Cu Alloy Specimens. Degrees of undercooling are (a) 10°K, (b) 100°K, (c) 200°K; magnification 100X (from Reference 10)

The EHD technique should lend itself to a variety of controlled undercooling experiments coupled with rapid solidification. As will be shown in Section 6, extremely fine atomized droplets (micron size and smaller) can be routinely produced in the EHD apparatus. Therefore, it should be possible to carry out classical undercooling experiments (where droplet size is small enough to assure the absence of impurity particles responsible for heterogeneous nucleation in a large fraction of the droplets) coupled with rapid solidification. Finally, it is anticipated that the very fine particles thus generated could be directly examined by TEM techniques.

## SECTION 3

### EXPERIMENTAL APPROACH

The approach taken on this program for the production of fine metal powders utilizes the electrohydrodynamic method of small particle generation as previously reported (Ref. 11). This section includes a basic description of EHD and the apparatus employed to generate microparticles.

#### 3.1 REVIEW OF ELECTROHYDRODYNAMICS

The basis of droplet generation from conducting liquid surfaces when the surface is stressed by intense electrical fields can be described with the aid of figure 2. An electric field is established at the surface of a conductive liquid by the application of a potential difference. Charges are generated at the surface of the liquid as shown in figure 2(a). When the electric field is sufficiently large ( $\sim 10^7$  volts/meter), the electrostatic force exerted on the liquid surface can pull the liquid into the configuration shown in figure 2(b). The increased curvature at the liquid surface results in a higher electric field existing near the apex, as shown in figure 2(c). As a critical value of electric field is approached, the electrostatic forces can overcome the surface tension forces holding the liquid together. When this occurs, the liquid surface disrupts and charged liquid droplets are emitted as illustrated in figure 2(d). The droplets are subsequently accelerated by the electric field and emitted from the droplet generator.

To achieve fields sufficiently high to generate droplets at reasonably low applied voltages (e.g., 3 to 20 kilovolts), geometries having very small dimensions are used. Consider a conducting liquid at the tip of a capillary needle whose tip dimension is on the order of 300  $\mu\text{m}$  or

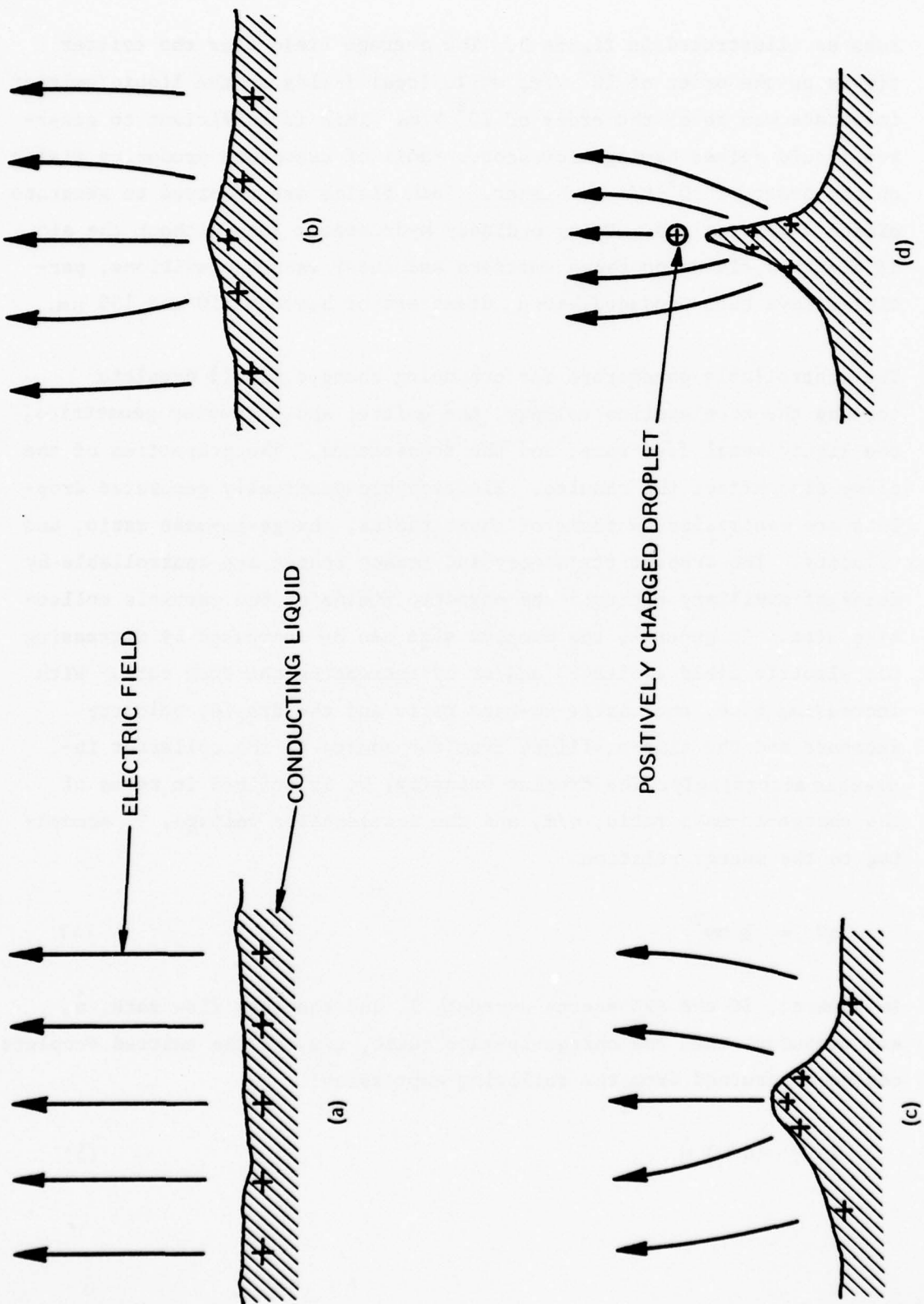


Figure 2. Electrohydrodynamic Generation of Charged Droplets

less as illustrated in figure 3. The average field over the emitter tip is on the order of  $10^7$  V/m, while local fields at the liquid/emitter interface can be of the order of  $10^8$  V/m. This is sufficient to generate liquid spikes having microscopic radii of curvature producing fields on the order of  $10^9$  V/m or higher. Such fields are required to generate micron size droplets. Using ordinary hydrostatic jets without the aid of electric fields on these emitters and under vacuum conditions, particles have been produced having diameters of between 110 and 150  $\mu\text{m}$ .

The controllable parameters for producing charged liquid droplets include the acceleration voltage, the emitter and extractor geometries, the liquid metal feed rate, and the temperature. The properties of the alloy also affect the results. Electrohydrodynamically generated droplets are controlled in terms of their radius, charge-to-mass ratio, and velocity. The droplet trajectory and impact energy are controllable by means of auxiliary electric and magnetic fields at the particle collection site. In general, the droplet size can be increased by decreasing the electric field (voltage) and/or by increasing the flow rate. With increasing size, the charge-to-mass ratio and the droplet velocity decrease and the time-of-flight from the source to the collector increases accordingly. The droplet velocity,  $v$ , is defined in terms of the charge-to-mass ratio,  $q/m$ , and the acceleration voltage,  $V$ , according to the energy relation

$$qV = \frac{1}{2} mv^2 \quad (4)$$

In general, if the EHD source current,  $I$ , and the mass flow rate,  $\dot{m}$ , are measured, then the charge-to-mass ratio,  $q/m$ , of the emitted droplets can be determined from the following expression:

$$I = (q/m) \dot{m} \quad (5)$$

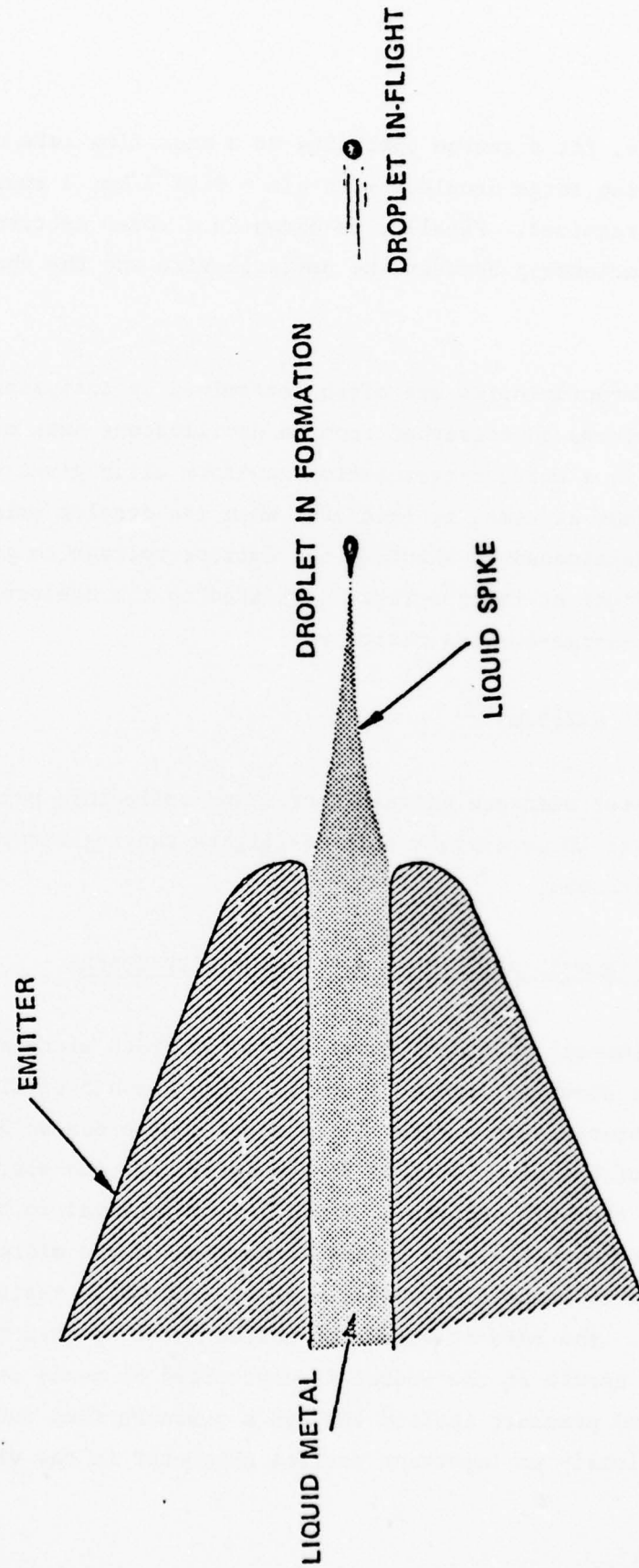


Figure 3. Electrohydrodynamic Droplet Generator

For example, for a source operating at a mass flow rate of  $10^{-5}$  kg/sec and producing large droplets with  $q/m = 0.01$  C/kg, a source current of  $0.1 \mu\text{A}$  is required. Finally, as shown in a later section, there is a direct relationship between the particle size and the charge-to-mass ratio.

Droplet characteristics are often determined by analyzing time-of-flight (TOF) waveforms photographed from an oscilloscope data display. The TOF trace is a current-versus-time waveform which gives the current at the collector at time,  $t$ , initiated when the droplet emission is abruptly terminated by shorting the emitter voltage to ground. The time-of-flight of the droplets is related to the collector distance,  $d$ , and their charge-to-mass ratio by:

$$t_f = d(2qV/m)^{-\frac{1}{2}} \quad (6)$$

For a 1 meter distance between source and collector, particles ranging from  $10^{-2}$  to  $10 \mu\text{m}$  exhibit time-of-flights ranging between  $10^{-3}$  and  $5 \times 10^{-2}$  seconds.

### 3.2 EXPERIMENTAL APPARATUS, THE FEASIBILITY MODEL

The experimental apparatus developed to generate microparticles in this program is shown in figures 4 and 5. With the aid of figure 4, operational features of the feasibility model source can be briefly described. (Details of the microparticle source design and its operation are discussed in the next section.) The alloy or material to be processed is placed in the crucible or reservoir portion of the microdroplet source and melted by means of suitable heaters (generally resistive heaters are used). The rate at which the molten metal is then delivered to the capillary nozzle at the source is controlled by means of an adjustable gas (argon) pressure applied through a pressure feed tube. Thus, pressure is clearly an important control parameter in the microdroplet

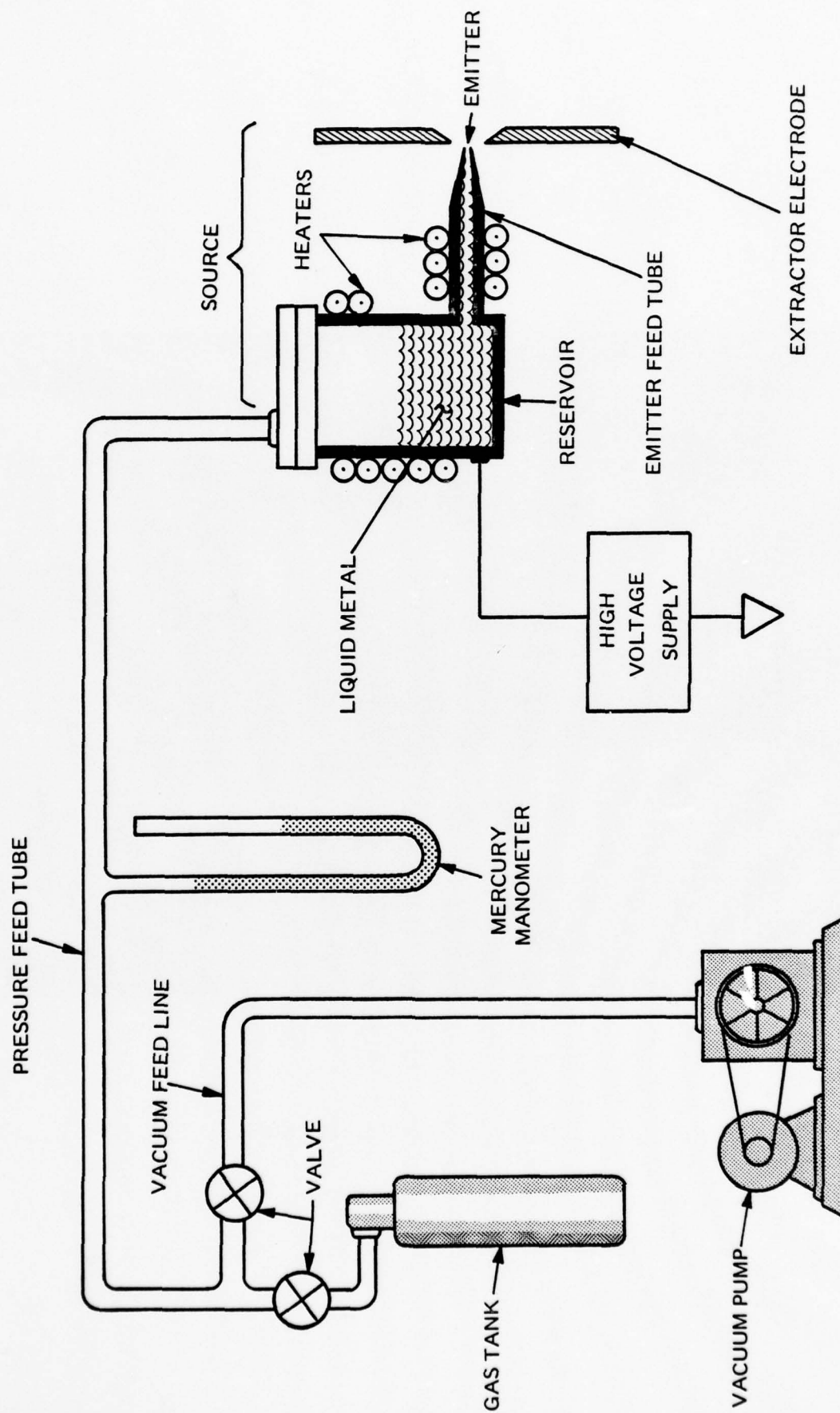


Figure 4. Feasibility Model Source Operations Diagram

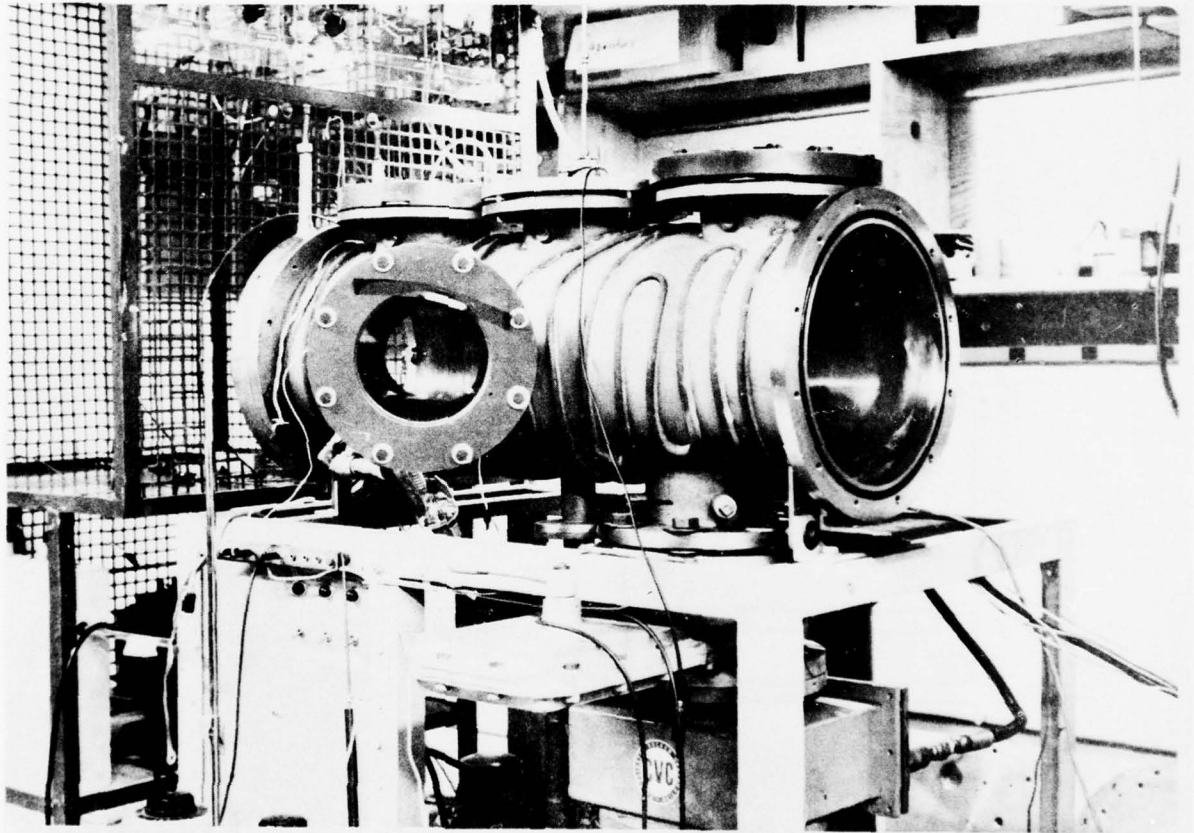


Figure 5. Feasibility Model

generation process. The pressure is controlled and varied as necessary using a small roughing pump in conjunction with the pressure system and valves shown in figure 5.

When the molten metal arrives at the nozzle tip, it enters a region of intense electrostatic field provided by a source of high potential. Once a desired flow rate of the molten material is established in the range from  $10^{-8}$  to  $10^{-6}$  kg/sec, the size of the emitted microdroplets can be further controlled by the magnitude of high voltage applied, which, as previously indicated, is also an important control parameter. Although pressure and voltage are the controls available to the system operator, these translate into the more meaningful parameters of mass flow rate and electric field.

The materials processing chamber of the feasibility model consists of a cylindrical vacuum vessel which is 1 meter long and  $\sim 0.3$  meter in diameter (see figure 5). This chamber is equipped with seven access ports for probing and diagnostics. These ports were used to introduce small particle sample collectors, located on a swivel arm, in the flight path of the droplets generated at the source. The chamber is also equipped with a copper liner which can be cooled with water or liquid nitrogen to achieve a lower vacuum or provide a low temperature environment. The chamber can be evacuated to an operational level ( $10^{-5}$  torr) in a short time (1200 to 1800 seconds) using one 0.1525m (6 inch) diffusion pump. In its present arrangement, the processing vessel is configured so that the droplet beam is ejected horizontally. For symmetry, ease of collection, and other reasons, it may be more advantageous to orient the processing chamber in a vertical position in the future.

Finally, the diagnostic portion of the feasibility model includes time-of-flight instrumentation to study droplet beam properties, and includes various monitoring systems to measure and identify droplet source current emission, electrode drain currents, nozzle, and reservoir temperatures.

An electrical schematic showing the essential monitoring and control features for microparticle sources operated with the Laboratory Feasibility Model (LFM) is shown in figure 6. The nozzle power supply (0 to 25 kV) is used to provide the positive potential required to generate and accelerate the molten metal particles. The extractor electrode may be grounded or operated at a negative potential. Application of a negative potential (0 to 6 kV) on the extractor electrode is preferred to prevent secondary electrons from bombarding the nozzle tip. Standard analog meters (0 to 1 mA) are used to monitor the nozzle, extractor, and collector currents as shown in figure 6. The nozzle and reservoir (crucible) heaters are controlled by manually operated variacs connected to the low potential side of the circuit. These controls are protected from the high voltage portion of the circuit by stepdown isolation transformers. Conventional pyrometer gages are used to process thermocouple signals which display feed tube and reservoir temperatures.

Further testing and evaluation of the LFM will lead to the design of the Engineering Model. It is planned to continue variable parameter testing with the Laboratory Feasibility Model for different and new materials, as well as determine the preliminary feasibility of new source and collector configurations.

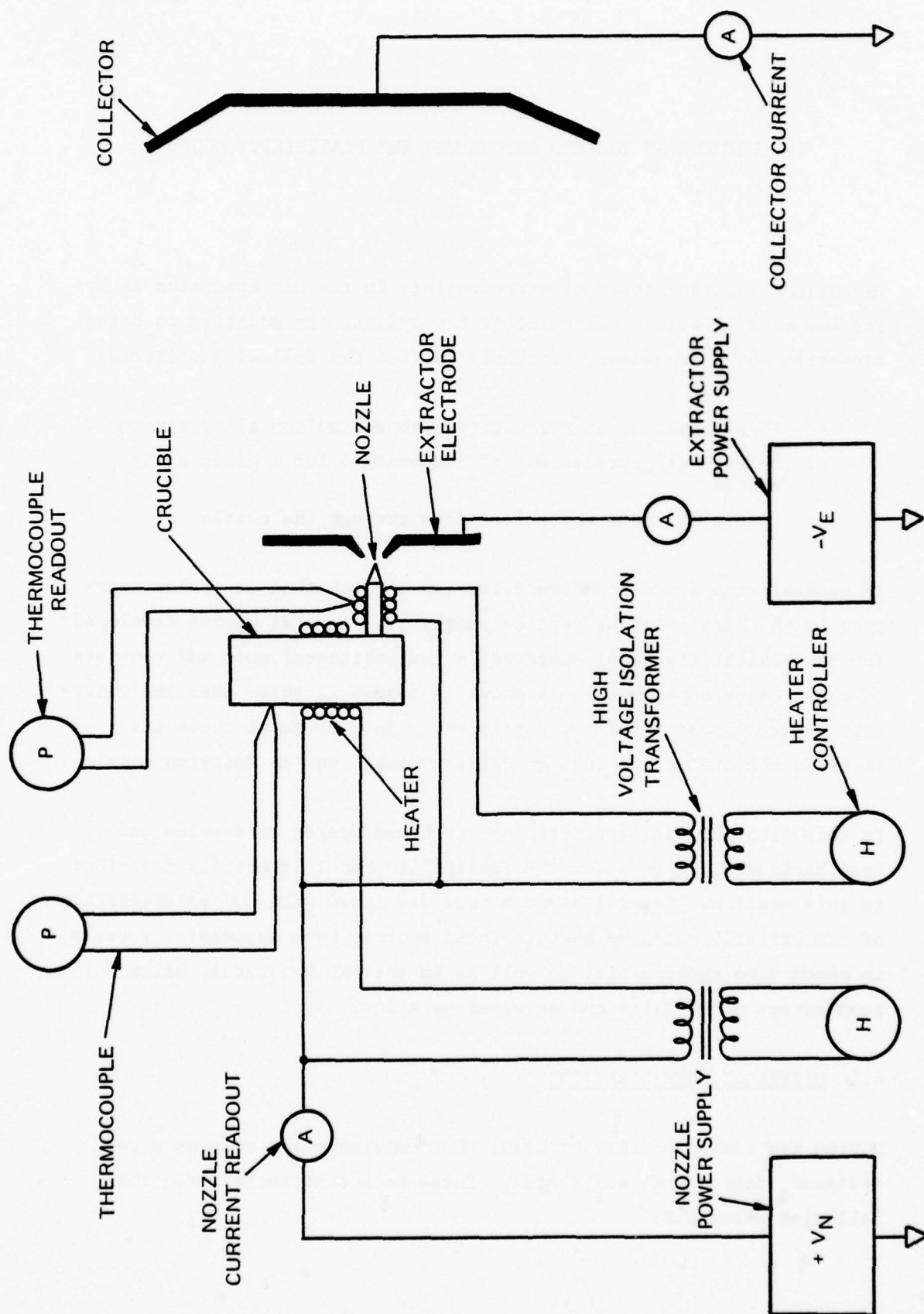


Figure 6. Electrical Schematic for Microparticle Source Operation

## SECTION 4

### DEVELOPMENT OF THE EHD SOURCE FOR THE FEASIBILITY MODEL

The source for generation of microdroplets in the EHD apparatus is by far the most important component of the system. In addition to being versatile and inexpensive, it should fulfill the following criteria:

- a. Show little or no reactivity with the molten alloy stream
- b. Operate at a predetermined temperature for a given alloy system
- c. Permit accurate control of flow through the nozzle

In general, the source configuration can be such that it either operates in the horizontal or vertical mode. The initial source developed for the Feasibility Model operates in the horizontal mode and consists of three major components. As shown in figure 7, these are: the reservoir system for maintaining a sufficient supply of metal above its liquidus temperature, a feed or delivery tube, and an emission nozzle.

In this program, the systematic approach undertaken to develop and test horizontal sources for the Feasibility Model is briefly described in this section. Several sources were developed with due consideration of the criteria outlined above. These sources were successfully tested in bench-type experiments, as well as in the EHD apparatus, using a low temperature model alloy and an aluminum alloy.

#### 4.1 MATERIALS CONSIDERATIONS

During the course of this program, four microdroplet sources were designed, fabricated, and tested. These were constructed from the following materials:

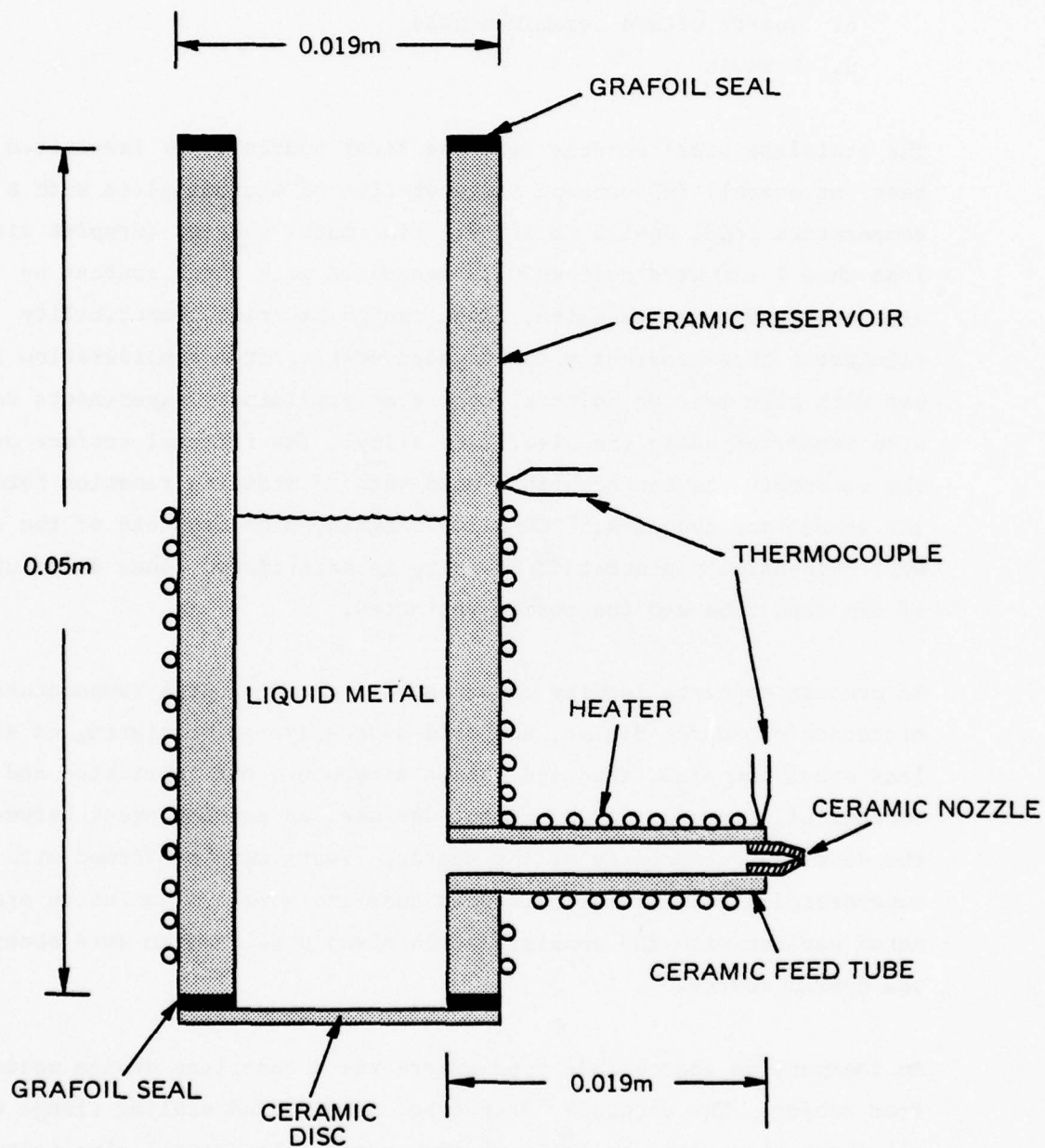


Figure 7. Schematic Diagram of the Horizontal Source in the Feasibility Model (clamping arrangement not shown)

- a. Stainless steel with a tungsten nozzle
- b. Stainless steel - ceramic hybrid
- c. Quartz with a ceramic nozzle
- d. Ceramic

The stainless steel sources were the first source types fabricated to test the overall EHD concept in generation of microdroplets with a low temperature model Sn-15% Pb alloy. Fine metal powders (droplet sizes less than 1  $\mu\text{m}$ ) were successfully generated with these sources by electrohydrodynamic emission. Even though material compatibility eliminated these sources with tungsten nozzles from consideration for use with high melting point alloys, some preliminary experiments were also performed using the Al-4.5% Cu alloy. The internal surface of the reservoir was coated with a mold wash to minimize reaction between the source and the Al-4.5% Cu alloy. Again, microdroplets of the alloy were successfully generated; however, as anticipated, some dissolution of the feed tube and the nozzle was noted.

To pretest concepts leading toward an all ceramic, high temperature, microdroplet source design, a hybrid source system consisting of stainless steel and  $\text{Al}_2\text{O}_3$  feed and nozzle components was fabricated and successfully tested.  $\text{Al}_2\text{O}_3$  cement was used as bonding agent between the different components of the source. Tests were performed with superheated Al-4.5% Cu alloy. Feed tube and nozzle dissolution problems noted earlier with the completely stainless steel source were absent in the hybrid source.

An inexpensive source made from quartz was a one-piece design molded from tubing. The crucible, feed tube, nozzle, and sealing flange were all glass blown into an integral structure. The overall simplicity and low cost of fabrication was offset by its fragility and perhaps limited versatility in containing a wide selection of alloys. However, the powder producing tests were successful and this source material could be used in special cases.

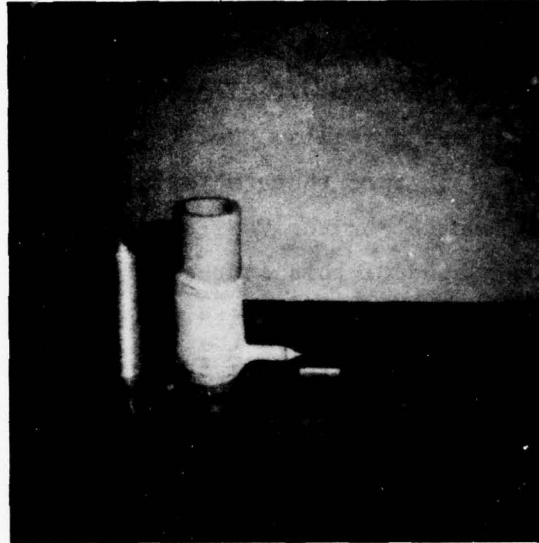
Finally, an all ceramic source was developed and successfully tested in this program. The basic design is flexible enough to accommodate construction of the source from a variety of ceramic materials, including mullite, alumina, and beryllia. Nozzles with desired orifice diameters of 25 to  $\sim 175 \mu\text{m}$  of these materials are available. The initial all-ceramic source for the Feasibility Model was of mullite. Figure 8 shows photographs of this source before and after assembly. Figure 8(a) shows the source proper with an Al-4.5% Cu alloy slug prior to loading, a ceramic feed tube, and several grafoil gaskets used for sealing purposes. The complete assembly is shown in figure 8(b). This source was successfully used to generate droplets of the Al-4.5% Cu alloy in the EHD apparatus. A structural analysis of the powders and splatted specimens produced is presented in a subsequent section.

Finally, it should be noted that work is presently underway to test an all-ceramic source designed for operation in the vertical mode. It is anticipated that this source would completely eliminate the use of gaskets in the lower extremity of the source.

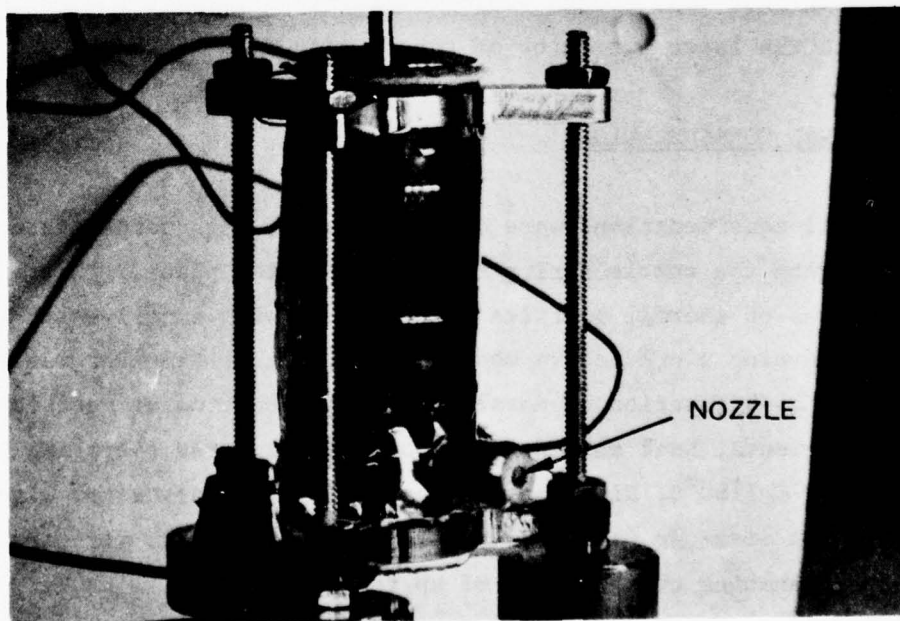
#### 4.2 THERMAL CONSIDERATIONS

The thermal considerations were dictated by the high temperature source designed with the nozzle firing in the horizontal plane. Theoretical calculations of thermal profiles were coupled with experimental measurements to develop a predictive model for achievable temperatures at the nozzle tip as a function of nozzle material, location of resistance heating elements, heat shields, and power input. For operating temperatures below  $\sim 1100^{\circ}\text{C}$ , Nichrome V with Ni-20% Cr alloy heater wire of  $\sim 5 \times 10^{-4}$  m diameter was used. Elements with tantalum wire are available for operating temperatures of up to  $2500^{\circ}\text{C}$ .

In the theoretical work, a heat balance was performed for conductive and radiative cooling from a conical nozzle. The heat balance equation



(a)



(b)

Figure 8. Photographs of the All-Ceramic (mullite) Source in the Feasibility Model. (a) and (b) show the source before and after assembly, respectively.

was solved numerically using the appropriate boundary conditions. An important outcome from this work was that materials considerations, e.g., alumina, beryllia, temperature of the alloy in the reservoir, and the use of a heat shield around the nozzle are essential for operation with a given alloy system if premature solidification of the alloy in the nozzle is to be avoided. Thermal measurements and experimental observations with the aluminum alloy in the Feasibility Model have shown good correlation with the numerical calculations. The future all-ceramic high temperature alloy sources are presently being designed, based on the appropriate thermal profiles from the mathematical model.

#### 4.3 FLOW CONTROL

The flow control in the source has as its primary function the delivery of controlled temperature alloy from the reservoir to the tip of the extraction nozzle. A schematic of the basic system for pressurizing the top of the melt is shown in figure 5. A suitable system, one that employs grafoil gaskets, was developed for sealing the top of the reservoir from the vacuum system. Inert gas on top of the melt is presently utilized to create a pressure gradient for controlled flow of the metal through the nozzle. As previously noted, the source and flow control system on the Feasibility Model have been successfully used with an aluminum alloy. It is felt that this aspect of the apparatus would need further refinement, and work is presently underway in this direction. Some basic considerations of the flow rate control through the nozzle are discussed below.

In general, a minimum pressure differential is required for initiation of flow from the nozzle tip. Since the nozzle tip is in vacuum, then the required pressure becomes:

$$p = \frac{2\gamma}{r} \quad (7)$$

where  $\gamma$  is surface tension and  $r$  is the inner radius of the nozzle. Equation (7) is written for the case of complete non-wetting between the alloy and the nozzle material.

After the flow has been established, the surface tension will no longer restrain the flow out of the nozzle. The pressure that initiated the flow has to be eliminated. The two possible approaches for adjusting the pressure are an instantaneous release of the pressure in the source or a pressure drop associated with the initiation of flow.

The instantaneous release of pressure after the surface tension has been overcome is difficult to achieve with a control system that has to operate with small time constants. It is therefore more logical to consider building a flow pressure drop into the system. The appropriate pressure drop in the nozzle can be generated by either reducing the diameter of the nozzle throughout its length or at its tip only. The former approach appears to be more practical due both to commercial availability of ceramic nozzles, as well as the need for extremely small calculated tip diameters in the latter case. Using the Hagen-Poiseuille law for laminar steady-state flow of incompressible fluids in tubes, the appropriate length-to-diameter ratio of the nozzles can be readily determined. The pressure drop due to frictional forces in the nozzle is set equal to the pressure differential required at the nozzle tip to overcome surface tension forces (Eq. (7)) yielding

$$\frac{8\eta L \dot{m}}{\pi \rho r^4} = \frac{2\gamma}{r} \quad (8)$$

where  $\eta$ ,  $\rho$ , and  $\dot{m}$  are the viscosity, density, and mass flow rate of the alloy, respectively, and  $r$  and  $L$  are the radius and length of the nozzle.

Equation (8) can also be used to give the minimum or cut-off mass flow rate at initiation of flow after the surface tension forces are overcome

upon application of pressure on top of the melt in the reservoir.

Finally, nozzle geometry can be deduced by rearranging Eq. (8):

$$\frac{r^3}{L} = \frac{4\nu}{\pi\gamma} \dot{m} \quad (9)$$

where  $\nu$  is the kinematic viscosity of the liquid alloy given by  $\eta/\rho$ .

For example, using the following parameters for an Al-4.5% Cu alloy flowing through an alumina nozzle:

$$\nu = 10^{-6} \text{ m}^2/\text{sec}$$

$$\gamma = 0.84 \text{ N/m}$$

$$\dot{m} = 5 \times 10^{-7} \text{ kg/sec}$$

and a nozzle diameter of  $3.81 \times 10^{-5} \text{ m}$ , a required nozzle length of  $\sim 0.01 \text{ m}$  (1 cm) is calculated from Eq. (9).

## SECTION 5

### HEAT FLOW DURING SOLIDIFICATION OF THE MICRODROPLETS

#### 5.1 POWER LOSS AND SOLIDIFICATION TIME

As the spherical liquid metal droplets travel from the emitter to the collector, they will lose energy by radiation, and, consequently, will undergo cooling. If an inert gas is introduced into the chamber, then the droplets will also lose energy by convection, which will increase the rate of heat extraction from their surface. The inert gas, however, will also add energy to the droplet, due to the frictional forces acting on the droplet. For the particular type of droplets, droplet velocities, droplet radii, and inert gases considered in the EHD apparatus, the energy lost by convection will exceed that gained by friction.

In general, the liquid droplets will be initially at a temperature above the liquidus temperature of the alloy and so, while they are in transit, they will first lose their superheat and then begin to solidify below or at the liquidus temperature, depending on whether they undercool or not. An important task is to determine whether, for a given set of droplet parameters (e.g., droplet size, velocity, etc.) a droplet will arrive at the collector in the completely liquid, partially solid, or completely solid state. Also, the attainable range of cooling rates prior to and during solidification should be established. Finally, the droplets traveling at high velocities gain thermal energy upon impact with the collector. This must be taken into consideration to determine the conditions under which partial or complete remelting of a solidified particle may occur and whether deceleration should be imposed at the collector to minimize this energy gain.

In the following paragraphs, a preliminary analysis is presented of the overall power loss from a droplet in flight and the time necessary

for its complete solidification. The latter is established on the basis of the following assumptions:

- The droplet is initially at its melting temperature.
- The droplet solidifies at a single temperature.
- No temperature gradient exists in the droplet, cooling is Newtonian.

The third assumption essentially requires that the Biot number,  $Bi$ , satisfy the following inequality:

$$Bi = \frac{h_{eff} a}{k} \lesssim 0.01 \quad (10)$$

where,

- $h_{eff}$  = effective heat transfer coefficient at the droplet surface for combined radiative and convective cooling
- $a$  = droplet radius
- $k$  = thermal conductivity of the droplet

These assumptions are reasonable (Ref. 4) considering the small size of the droplets generated in the EHD apparatus and the fact that the effective heat transfer coefficient in the system is relatively small.

Details of radiative and convective cooling of the droplets, solidification times, cooling rates for pure metals, and an alloy freezing over a range of temperatures and the reheating of droplets on impact with the collector are presented below and in the following subsections.

The power lost by the droplet during flight due to radiation and convection, and the power gained by friction are  $P_R$ ,  $P_C(t)$ , and  $P_f(t)$ , respectively. Here,  $t$  denotes time. The net power,  $P_T$ , released by the droplet is then

$$P_T(t) = P_R + P_C(t) - P_f(t) \quad (11)$$

The energy given up by the droplet during solidification is

$$E = \int_0^{\tau} P_T(t) dt \quad (12)$$

where  $\tau$  = solidification time. The energy lost by the droplet during complete solidification is also given by:

$$E = mH \quad (13)$$

where  $m$  = mass of the droplet and  $H$  = heat of fusion of the alloy.

Combining Eqs. (11), (12), and (13) then yields the following equation for the solidification time:

$$P_R \tau + \int_0^{\tau} P_C(t) dt - \int_0^{\tau} P_f(t) dt = mH. \quad (14)$$

Since Eq. (14) is an implicit equation in  $\tau$ , it therefore must be solved graphically, or numerically, for  $\tau$ . The value of  $\tau$  which satisfies Eq. (14) will represent the solidification time only if the droplet solidifies before it reaches the collector surface.

If  $t_f$  denotes the time taken for the droplet to go from the emitter to the collector (flight time), which are a distance  $d$  apart, then the droplet will solidify before reaching the collector if

$$\tau \leq t_f \quad (15)$$

If no gas occupies the chamber, then  $P_C = P_f \equiv 0$ , so that the solidification time becomes

$$\tau = \frac{mH}{P_R} \quad (16)$$

If the initial temperature of the droplet is higher than its melting temperature, then the droplet will lose energy in two successive stages. In the first stage, the droplet temperature drops from its initial value to the melting temperature, and the rate of the temperature drop, or, cooling rate is given by

$$\frac{dT}{dt} = \frac{P_T(t)}{m C_p} \quad (17)$$

where  $C_p$  = specific heat of the alloy. Since  $P_T$  is, in general, time-dependent, therefore, so will  $dT/dt$  be time-dependent. In the second stage, the droplet will solidify as noted above.

For a given droplet superheat,  $\Delta T$ , the time to reach the melting temperature can be calculated from Eq. (17). This time should then be added to the solidification time,  $\tau$ , in Eq. (14) or (16) to establish whether the droplet would be completely solid when it arrives at the collector.

## 5.2 RADIATION COOLING

The power lost by a spherical droplet due to radiation is given by

$$P_R = 4\pi a^2 \epsilon \sigma_s (T^4 - T_o^4) \quad (18)$$

where,  $a$ ,  $T$ , and  $T_o$  are the radius and temperature of the droplet and the temperature of the environment, respectively;  $\sigma_s$  = Stefan-Boltzmann constant, and  $\epsilon$  = total hemispherical emissivity of the droplet surface. Now, the emissivity,  $\epsilon$ , is generally determined from experiment, and is critically dependent on the nature of the emitting surface, i.e., whether the surface is rough, smooth, oxidized, etc. Thus, Eq. (18) is generally applicable to a macrosized droplet, since the surface characteristics of a macrosized particle can be described as rough,

smooth, oxidized, etc. Suppose, however, that the droplet is micro-size, i.e., has a diameter of the order of 1 micron or less. Then the validity of Eq. (18) becomes questionable, since the diameter of the droplet is itself smaller than the discernible irregularities found on the surface of a macrosized particle. Furthermore, the power that escapes from a microsize sphere can be expected to originate throughout a significant portion of the sphere's interior rather than from its outer shell, as implied by Eq. (18).

By assuming that the temperature,  $T$ , of the droplet is constant throughout its interior, and that the surface of the droplet is optically smooth, then, by summing up the radiation from the differential elements of the droplet, an expression for the spectral power (i.e., power at a single frequency or wavelength) radiated from a microsize sphere has been derived. The power radiated from the microsphere in the frequency interval  $\nu$ ,  $\nu + d\nu$ , is given by

$$P_{R\nu} = \frac{8\pi^2 a^2 h_p}{c^2} f(n, \beta_c, \alpha a) \frac{\nu^3 d\nu}{e^{\frac{h\nu}{kT}} - 1} \quad (19)$$

where,

$$f(n, \beta_c, \alpha a) = n^2 \left[ \sin^2 \beta_c + \frac{e^{-2\alpha a}}{\alpha a} \left(1 + \frac{1}{2\alpha a}\right) - \frac{e^{-2\alpha a \cos \beta_c}}{\alpha a} \left(\cos \beta_c + \frac{1}{2\alpha a}\right) \right]$$

Here,  $h_p$ ,  $c$ ,  $k$  are Planck's constant, the speed of light in vacuum, and Boltzmann's constant, respectively. Also,  $n$  and  $\alpha$  are the index of refraction (real part) and optical absorption coefficient, respectively, of the droplet. Finally,  $\beta_c$  is the critical angle of reflection within the droplet, given by

$$\sin \beta_c = \left\{ 1 + \frac{1}{2} \left[ K - 1 + \sqrt{\left(\frac{\sigma}{2\pi\epsilon_0}\right)^2 \frac{1}{\nu^2} + (K - 1)^2} \right] \right\}^{-\frac{1}{2}} \quad (21)$$

where,  $K$  and  $\sigma$  are the dielectric constant (dimensionless) and electrical conductivity, respectively, of the droplet, and  $\epsilon_0$  = permittivity of free space =  $8.854 \times 10^{-12}$  farads/meter. Here,  $K \geq 1$  and  $0 \leq \beta_c \leq \pi/2$ . When  $\beta_c = 0$ , none of the radiation escapes the spherical droplet, and when  $\beta_c = \pi/2$ , all the radiation escapes the droplet.

Equation (19) is especially valid for a microsize droplet, since the temperature of a microdroplet can be considered uniform throughout.

The index of refraction,  $n$ , and absorption coefficient,  $\alpha$ , are also frequency dependent. This dependency is best determined experimentally. Analytical expressions for  $n$  and  $\alpha$  can be derived from electromagnetic theory, but they do not yield values that agree with experiment, for all values of frequency.

### 5.3 CONVECTIVE COOLING

The amount of power lost by a droplet due to convection depends critically on the particle-interaction regime, i.e., whether the flow is viscous, slip, or molecular. In the case of viscous flow, the convective power loss,  $P_c(t)$ , is given by

$$P_c(t) = 4\pi a^2 h_c(t) (T - T_0) \quad (22)$$

where,  $h_c(t)$  = convective heat transfer coefficient. A reasonably accurate description of  $h_c(t)$  (Ref. 12) is given by

$$h_c(t) = \frac{k'}{a} (1 + 0.3 R_e^{1/2} P_r^{1/3}) \quad (23)$$

where,

$$R_e = \text{Reynolds' No.} = 2a v(t) \rho' / \eta'$$

$$P_r = \text{Prandtl's No.} = C' \eta' / k'$$

Here,  $k'$ ,  $\rho'$ ,  $\eta'$ ,  $C'$  are the thermal conductivity, density, viscosity, and specific heat, respectively, of the chamber gas, and  $v(t)$  denotes the velocity of the droplet as it moves through the gas. The droplet velocity depends on the value of Reynolds' No. in the following way:

$$R_e > 1: \quad v(t) = v_o \left(1 + v_o \frac{K_1}{m} t\right)^{-1} \quad (24)$$

$$R_e < 1: \quad v(t) = v_o e^{-K_2/m t} \quad (25)$$

Here,  $K_1 = \pi a^2 \rho' C_D / 2$  and  $K_2 = 6\pi \eta' a / (1 + 1.222 L/a)$ , where,  $C_D$  = "drag coefficient" and  $L$  = mean free path of the gas molecules. Also,  $v_o$  = initial velocity of the droplet, and  $m$  = mass of droplet. In deriving Eqs. (24) and (25), the effect of gravity was ignored, and it was assumed that  $C_D$  was a constant.

The convective power loss in the slip and molecular flow regimes is not completely understood and needs further study. However, in the case of molecular flow, the convective power loss is generally expected to be negligible compared to the radiative power loss,  $P_R$ .

#### 5.4 CALCULATION OF SOLIDIFICATION TIME AND COOLING RATE

The two inert gases that would most likely be introduced into the chamber to achieve convective cooling are helium and argon. If helium is employed at room temperature ( $293^\circ\text{K}$ ), then viscous flow will occur when

$$a > \frac{1.9 \times 10^6}{p} \mu\text{m}$$

where,  $a$  = radius ( $\mu\text{m}$ ) of the spherical droplet and  $p$  = pressure ( $\text{N/m}^2$ ) inside the chamber. At atmospheric pressure, i.e.,  $p = 101,293 \text{ N/m}^2$ ,

it is seen that the droplet radius must be greater than  $\sim 19 \mu\text{m}$  in order to consider viscous flow. If argon gas is employed at room temperature, viscous flow will occur when

$$a > \frac{6.87 \times 10^5}{p}, \mu\text{m}$$

At atmospheric pressure, the droplet radius must exceed  $\sim 7 \mu\text{m}$  in order to use the viscous flow relationships. Since the representative droplet diameter being considered in this program is of the order of  $1 \mu\text{m}$  or less, therefore, the viscous flow regime will not be included in the present calculations.

Heretofore, all experiments in the EHD apparatus were carried out in vacuum. Therefore, the power generated by friction and the heat losses due to convection are ignored in the following calculations. The solidification time,  $\tau$ , for a droplet solidifying at a single temperature is given by Eq. (16), where  $P_R$  is given by Eq. (18). By combining Eqs. (16) and (18) and making use of  $m = 4\pi a^3 \rho / 3$ , the solidification time of a droplet becomes

$$\tau = \frac{\rho H a}{3\epsilon\sigma_s(T_m^4 - T_o^4)} \quad (26)$$

where,  $T_m$  = melting temperature of the droplet. Table II shows all pertinent metal parameters employed in the calculations for the four pure metals: Al, Cu, Fe, and Ni. Figure 9 shows the solidification time,  $\tau$ , versus the droplet radius,  $a$ , for the above four metals. The emissivity,  $\epsilon$ , was taken to be unity in all cases. Note that, for a  $1 \mu\text{m}$  diameter droplet of aluminum, the solidification time is approximately 4 milliseconds.

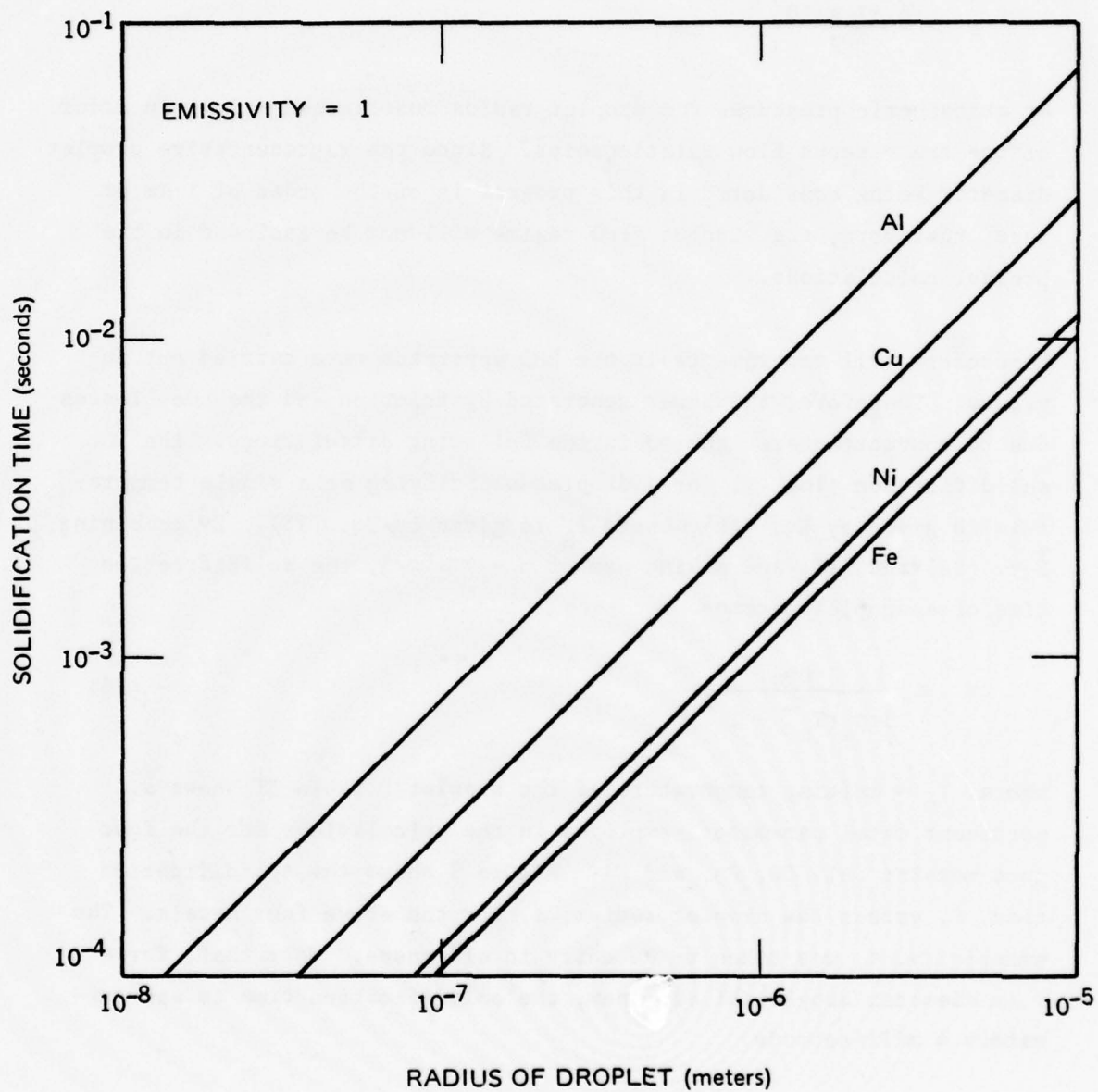


Figure 9. Solidification Time versus Droplet Radius, for Radiative Cooling

TABLE II

## LIQUID METAL PARAMETERS

Metal	Melting Temp. $T_m$ ( $^{\circ}\text{K}$ )	Specific Heat $C_p$ ( $\text{J/kg } ^{\circ}\text{K}$ )	Density $\rho$ ( $\text{kg/m}^3$ )	Heat of Fusion $H$ ( $\text{J/kg}$ )	Surface Tension $\gamma$ ( $\text{N/m}$ )
Al	933	1046	2382	$3.934 \times 10^5$	0.84
Cu	1356	494	7900	$2.051 \times 10^5$	1.30
Fe	1808	825	7000	$2.720 \times 10^5$	1.70
Ni	1728	733	7780	$2.348 \times 10^5$	1.67

As previously noted, the cooling rate prior to solidification, along with alloy composition, has an important influence on undercooling and the formation of crystalline and non-crystalline structures. If one assumes that the effective heat transfer coefficient for radiative cooling remains essentially constant (change in temperature of the droplet is not very large), then a single relationship between the average cooling rate prior to solidification and the solidification time of the droplet is obtained:

$$\frac{dT}{dt} = \frac{H}{C_p} \frac{1}{\tau} \quad (27)$$

Figure 10 shows the average cooling rate prior to solidification,  $\frac{dT}{dt}$ , versus the droplet radius for Al, Cu, Fe, and Ni. Note, that, for a 1  $\mu\text{m}$  diameter droplet of aluminum, the cooling rate prior to solidification is  $10^5$   $^{\circ}\text{K}/\text{second}$ .

As noted in Eqs. (1) and (2), segregate spacing in certain alloy systems solidifying over a temperature range can be directly correlated to the average cooling rate during solidification,  $(\frac{dT}{dt})_{\text{avg}}$ . An approximate

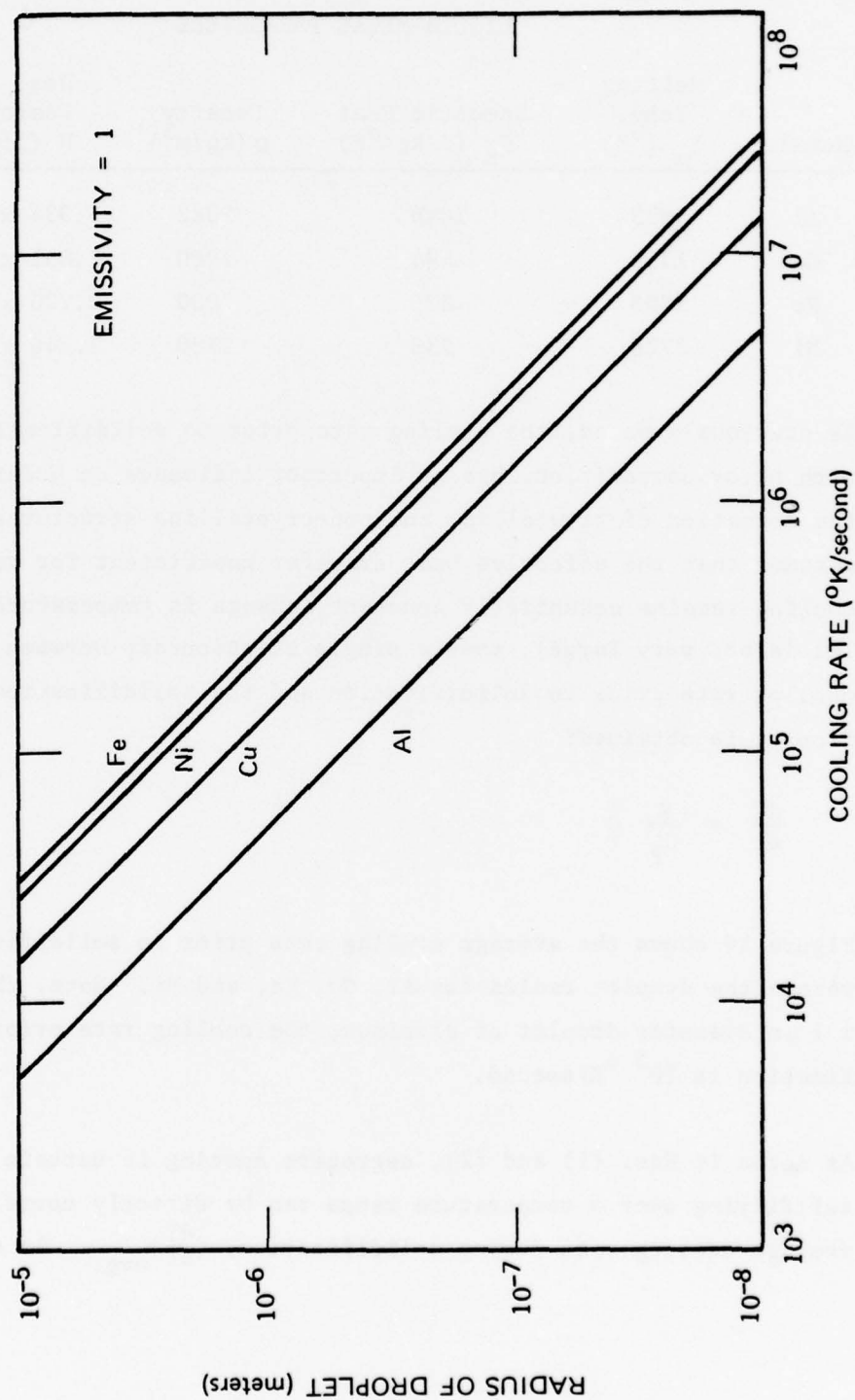


Figure 10. Cooling Rate versus Droplet Radius, for Radiative Cooling

method available for estimating average cooling rate during solidification is to use an average heat capacity,  $\bar{C}_p$ , of an alloy during solidification determined by linearizing the heat of fusion over the solidification temperature range. A corollary expression to Eqs. (26) and (27) is thus obtained:

$$\left(\frac{dT}{dt}\right)_{\text{avg.}} = \frac{3 h_{\text{eff}} (T - T_o)}{\rho \bar{C}_p a} = \frac{3 \epsilon \sigma_s (T^4 - T_o^4)}{\rho \bar{C}_p a} \quad (28)$$

where,  $h_{\text{eff}} = \epsilon \sigma_s (T + T_o) (T^2 + T_o^2)$  for the case of radiation cooling (deduced from Eqs. (18) and (26)), and  $T$  is an average temperature for the alloy in its solidification temperature range. Equation (28) is identical to Eq. (27) except that an average heat capacity,  $\bar{C}_p$ , during solidification is used instead of the heat capacity for the liquid.

For example, an Al-4.5% Cu alloy freezes over a temperature range of 100°K (liquidus temperature = 921°K, eutectic temperature = 821°K). The value of  $\bar{C}_p$  for this alloy is calculated from the values listed in Table II to be ~ 4980 J/kg °K. The corresponding average cooling rate during solidification of a 1 μm diameter droplet from Eq. (28) is  $1.62 \times 10^4$  °K/second.

The distance,  $s$ , travelled by the droplets during the solidification time,  $\tau$ , is given directly from Eq. (6):

$$s = v\tau = (2 V q/m)^{1/2} \tau \quad (29)$$

where,  $v$  = velocity (constant) of the droplet, and  $V$  = potential difference (volts) through which the charged droplets are accelerated. The charge-to-mass ratio,  $q/m$ , of the droplet (Ref. 13), as modified by experiments, is given by:

$$q/m = \frac{3(\gamma \epsilon_o)^{1/2}}{\rho a^{3/2}} \quad (30)$$

where,  $\gamma$  = surface tension of the liquid metal droplet, and  $\epsilon_0$  is the permittivity of free space. Table III shows the values of  $q/m$  and  $v$  for Al, Cu, Fe, and Ni, where the accelerating voltage was taken to be  $V = 10^4$  volts and the droplet radius,  $a = 0.5 \mu\text{m}$ . Figure 11 shows the distance,  $s$ , versus the droplet radius for the elements noted above. The calculated solidification times,  $\tau$ , can be obtained from figure 9. Note that, for a  $1 \mu\text{m}$  diameter aluminum droplet, the distance from the droplet source to the collector must be greater than 1.6 meters if the liquid droplet is to become solid before striking the collector. Experimental evidence obtained with Al-4.5% Cu alloy presented in the next section does not verify this prediction - particles larger than  $1 \mu\text{m}$  in diameter appeared to have completely solidified before striking the collector. This discrepancy may be due to our assumption that Eq. (30), determined from theory and experiment, is valid for these metallic systems.

TABLE III  
LIQUID DROPLET PARAMETERS  
(accelerating voltage = 10,000 volts)

Droplet	Mass $m$ (kg)	Charge/Mass $q/m$ (C/kg)	Initial Velocity $v_0$ (meters/second)
Al	$1.247 \times 10^{-15}$	9.714	440.79
Cu	$4.136 \times 10^{-15}$	3.644	269.96
Fe	$3.665 \times 10^{-15}$	4.702	306.68
Ni	$4.073 \times 10^{-15}$	4.193	289.61

### 5.5 HEATING OF MICROPARTICLES ON IMPACT

Microparticles that solidify before collection could conceivably remelt on impact, provided a sufficient amount of kinetic energy is available. It is important to correlate particle sizes to the energy required for

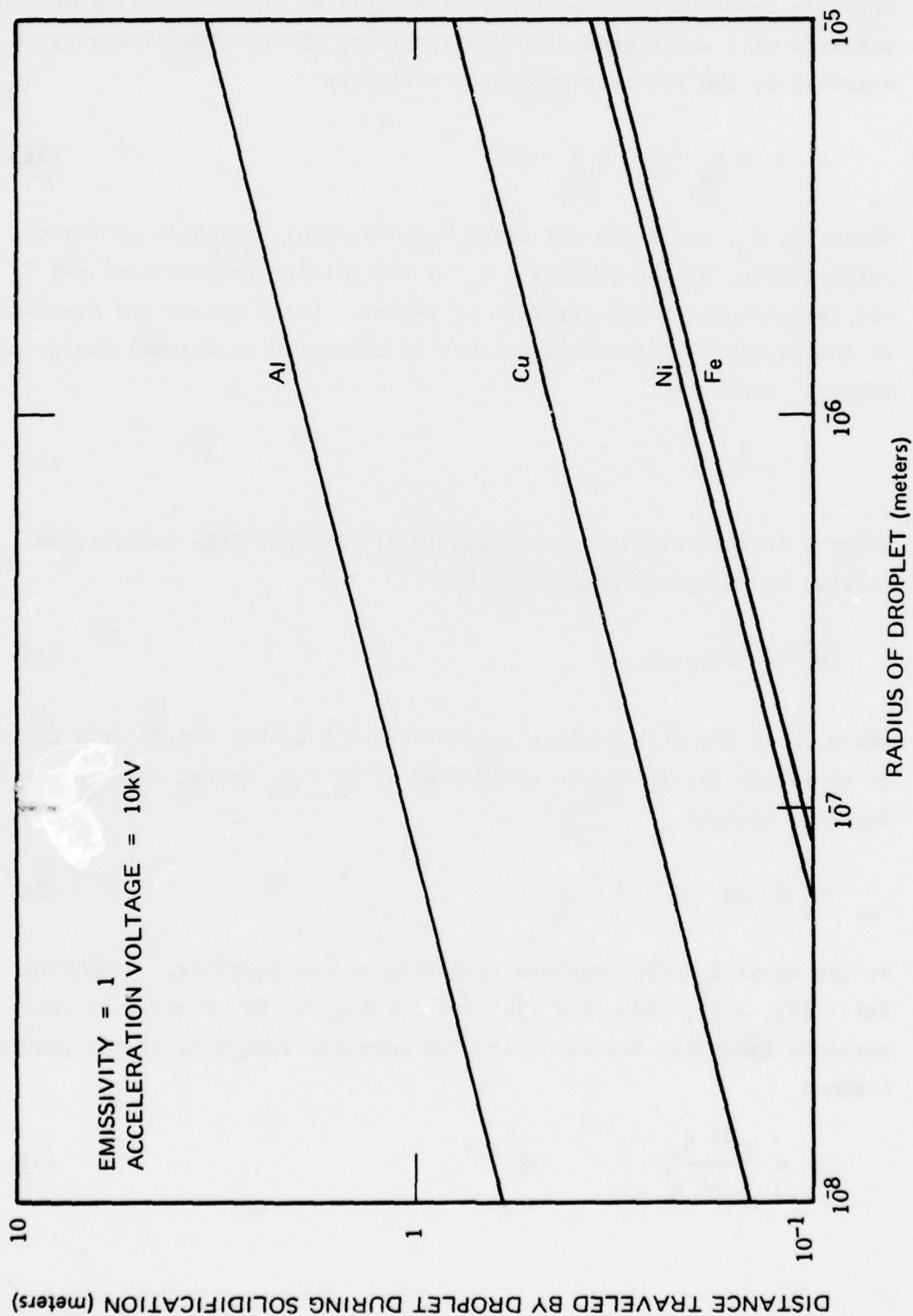


Figure 11. Distance Traveled by Droplets During Solidification versus Droplet Radius, for Radiative Cooling

particle remelt after impact with a substrate. Upon impact, a monatomic particle will experience complete remelting if the thermal energy,  $E$ , absorbed by the particle on impact satisfies

$$E \geq m C_p (T_m - T_o) + mH, \quad (31)$$

where,  $m$ ,  $C_p$ , and  $H$  are the mass, specific heat, and heat of fusion, respectively, of the particle,  $T_m$  is the melting temperature, and  $T_o$  is the temperature of the particle at impact. Let  $\beta$  denote the fraction of the particle kinetic energy that is converted to thermal energy on impact. Then

$$\frac{1}{2} m v^2 \beta = E, \quad (32)$$

where  $v$  is the velocity of the particle. The particle velocity is related to charge-to-mass ratio by:

$$v^2 = 2 V q/m \quad (33)$$

where,  $V$  is the accelerating potential and  $q$  is the charge on a particle. If we assume particles are solidified at  $T_o = T_m$  (worst case analysis), Eq. (31) becomes

$$E \geq mH \quad (34)$$

as the condition for complete remelting of the particle. Combining Eqs. (30), (32), (33), and (34) and letting  $d = 2a$ , where  $d$  is the particle diameter, the condition for complete remelting of the particle becomes

$$d \leq \left( \frac{72 \epsilon_o \gamma}{\rho^2 H^2} \right)^{1/3} (v\beta)^{2/3}. \quad (35)$$

This derivation is based on the assumption that Eq. (30) relating particle size to charge-to-mass ratio is valid.

The quantity  $(72 \epsilon_0 \gamma / \rho^2 H^2)^{1/3}$  is a constant and depends on the physical properties of the material. Table IV shows the values of this quantity for Al, Cu, Fe, and Ni.

TABLE IV  
VALUES OF  $(72 \epsilon_0 \gamma / \rho^2 H^2)^{1/3}$  FOR FOUR LIQUID METALS  
(MKS units)

Liquid Metal	$(72 \epsilon_0 \gamma / \rho^2 H^2)^{1/3}$
Al	$8.4800 \times 10^{-10}$
Cu	$6.8089 \times 10^{-10}$
Fe	$6.6864 \times 10^{-10}$
Ni	$6.8330 \times 10^{-10}$

Since the extreme values (for Al and Fe) differ by only 25 percent, the arithmetic mean value given by

$$\left( \frac{72 \epsilon_0 \gamma}{\rho^2 H^2} \right)^{1/3} = 7.202 \times 10^{-10} \text{ (MKS)}$$

will be employed in calculations of particle heating. The condition for the complete remelting of Al, Cu, Fe, or Ni particles on impact then becomes:

$$d \leq 7.202 \times 10^{-10} (v\beta)^{2/3} \text{ meters} \quad (36)$$

The curve in figure 12 represents a plot of Eq. (36) showing the variation of droplet diameter with the parameter  $v\beta$ . The area below this curve represents the region of complete remelting of the particles and the

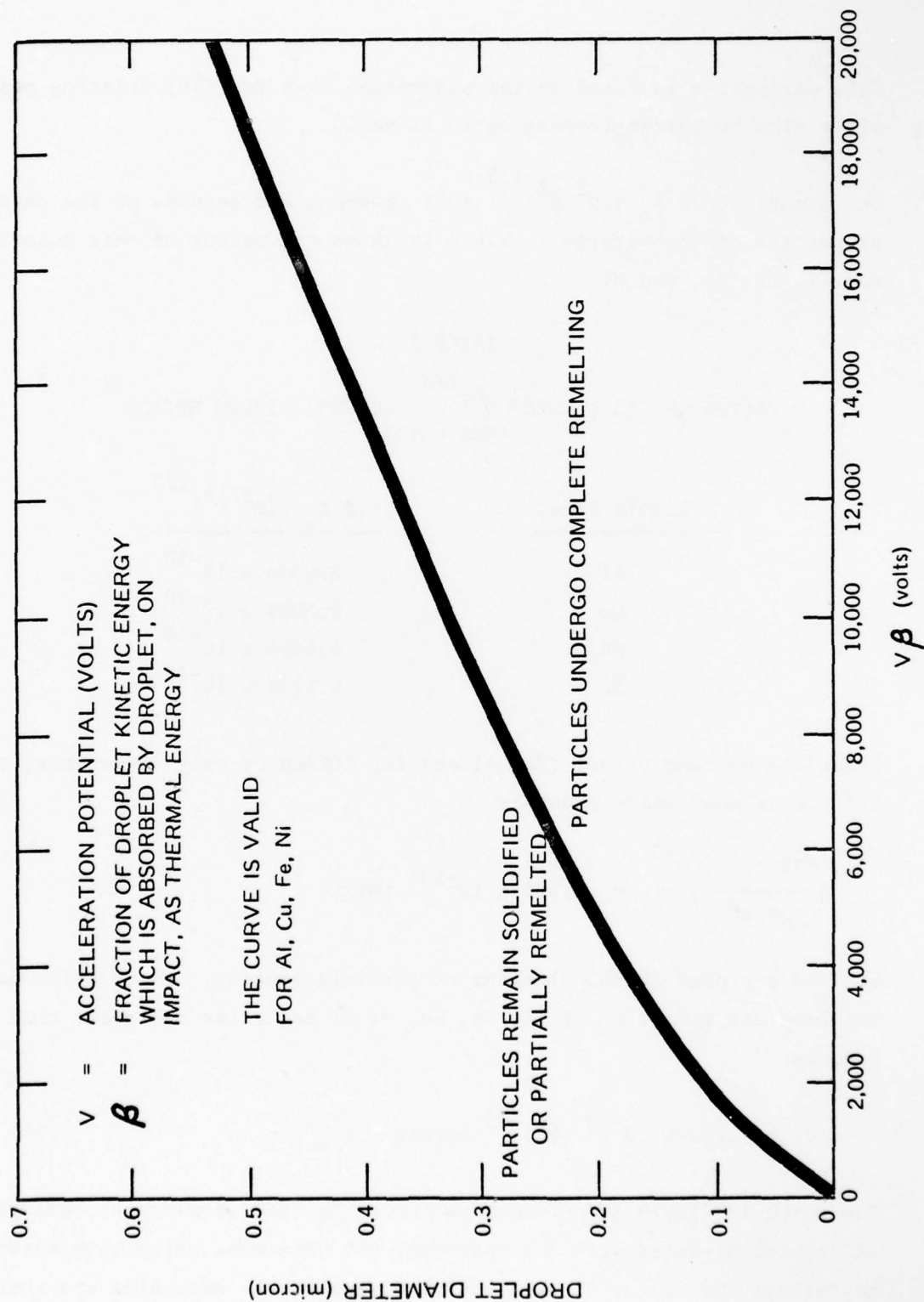


Figure 12. Conditions on Particle Heating Upon Impact

area above the curve represents the region where particles remain solidified or partially remelted. For example, suppose that the acceleration potential is 12 kV and that one-half the particle kinetic energy is absorbed as thermal energy at impact. Then, those particles having a diameter less than 0.24 micron will completely remelt and those having a diameter greater than 0.24 micron will remain solid or partially remelt.

The solidification region can be extended to smaller particles by employing deceleration techniques. Remelt of extremely fine particles (less than 0.5 micron) can be avoided by applying a positive deceleration potential to the collecting substrate. Thus, the thermal energy absorbed by the fine particles can be minimized and, as such, is not a limiting factor preventing the collection of fine particles in the solid state.

## SECTION 6

### EXPERIMENTAL RESULTS

All four sources, stainless steel, stainless steel-ceramic hybrid, quartz, and the all-ceramic source, were tested in the Feasibility Model EHD apparatus using a low temperature model alloy, Sn-15% Pb, and an aluminum alloy, Al-4.5% Cu. The Sn-15% Pb alloy was extensively used in bench-type tests to verify the electrohydrodynamic process for generating fine liquid droplets, as well as to develop the necessary process variables for operation of the apparatus. The Al-4.5% Cu alloy was also extensively utilized in preliminary experiments to:

- a. Demonstrate that the EHD apparatus can be successfully used to generate a large range of fine and coarse atomized droplets (from less than  $0.1\text{ }\mu\text{m}$  to over  $100\text{ }\mu\text{m}$ ), depending on the specific EHD source and the process variables employed
- b. Carry out a preliminary analysis of the range of structures, hence cooling rates, achievable in the apparatus
- c. Study techniques for collection of the fine atomized powders
- d. Demonstrate the capability of the apparatus to produce rapidly solidified splats on various substrates located in the flight path of the liquid droplets
- e. Investigate the possibility of producing thin, adherent, rapidly solidified coatings on substrates
- f. Develop specific specimen preparation procedures for examination of the resulting structures by electron microscope techniques

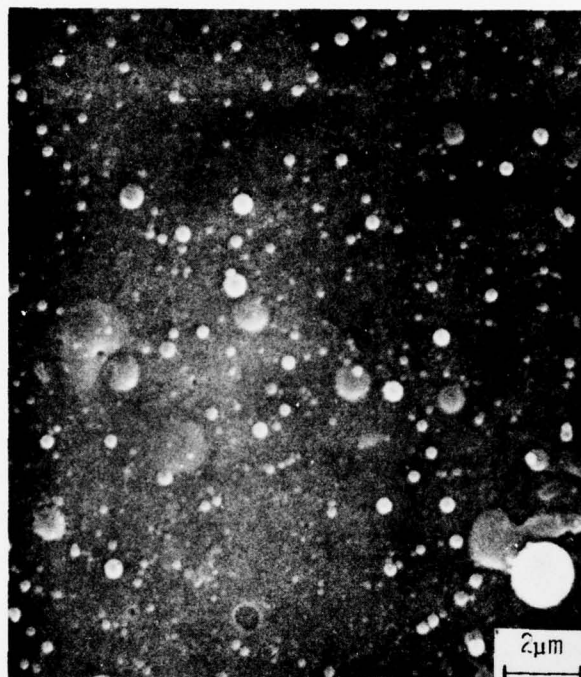
The results obtained to date are presented below under two general headings: atomization studies and splat cooling studies.

## 6.1 ATOMIZATION STUDIES

It was successfully demonstrated that the EHD apparatus can produce a large range of atomized droplets with a metallic source (stainless steel), a hybrid source (stainless steel-ceramic), a quartz source, and a non-metallic source (mullite). In these preliminary studies, heat flow during flight of the droplets was by radiative cooling only. Therefore, depending on the size of the droplets, their velocity, and the location of the collector, the droplets were partially or completely solidified in flight or arrived at the target as liquid.

Figures 13 and 14 show Secondary Electron Images (SEI) of Al-4.5% Cu powders collected on a vinyl cellulose substrate located in the flight path. Figures 13(a) and 13(b) show essentially fine atomized powders in the size range of less than 0.1 to 1.0  $\mu\text{m}$ . On the other hand, the size range of the powders in figure 14 is an order of magnitude larger ( $\sim 0.2$  to  $\sim 10 \mu\text{m}$ ). There is evidence that some of the coarser droplets arriving at the target penetrated into the vinyl cellulose - the light gray spheres in figure 13(b). Figures 13 and 14 also show that a soft target material, i.e., vinyl cellulose, can be successfully used to collect the very fine particles generated by EHD. Furthermore, the spheroidal geometry of most of the powders indicates that these were solidified in flight.

As noted above, collection of solidified fine droplets in the EHD apparatus does not appear to pose a serious difficulty. It should be specified that, since the atomized particles are charged, they could also be directed to specific targets in the EHD chamber for collection. On the other hand, coarse powders, e.g.,  $\sim 20$  to  $\sim 100 \mu\text{m}$  size range, have to be slowed down via a decelerator and collected at the far extremity of the chamber to allow them maximum flight time for solidification. Experiments to date, verifying earlier radiative heat flow calculations,



(a)



(b)

Figure 13. Secondary Electron Images of Fine Atomized Powders of Al-4.5% Cu Alloy Produced by the EHD Technique. These particles were rapidly solidified in flight. Collector (substrate) material was vinyl cellulose. (a) and (b) show powders in the size range of  $\sim 0.1 \mu\text{m}$  to  $\sim 1 \mu\text{m}$  produced with a non-metallic source at 5000X and 10,000X, respectively.

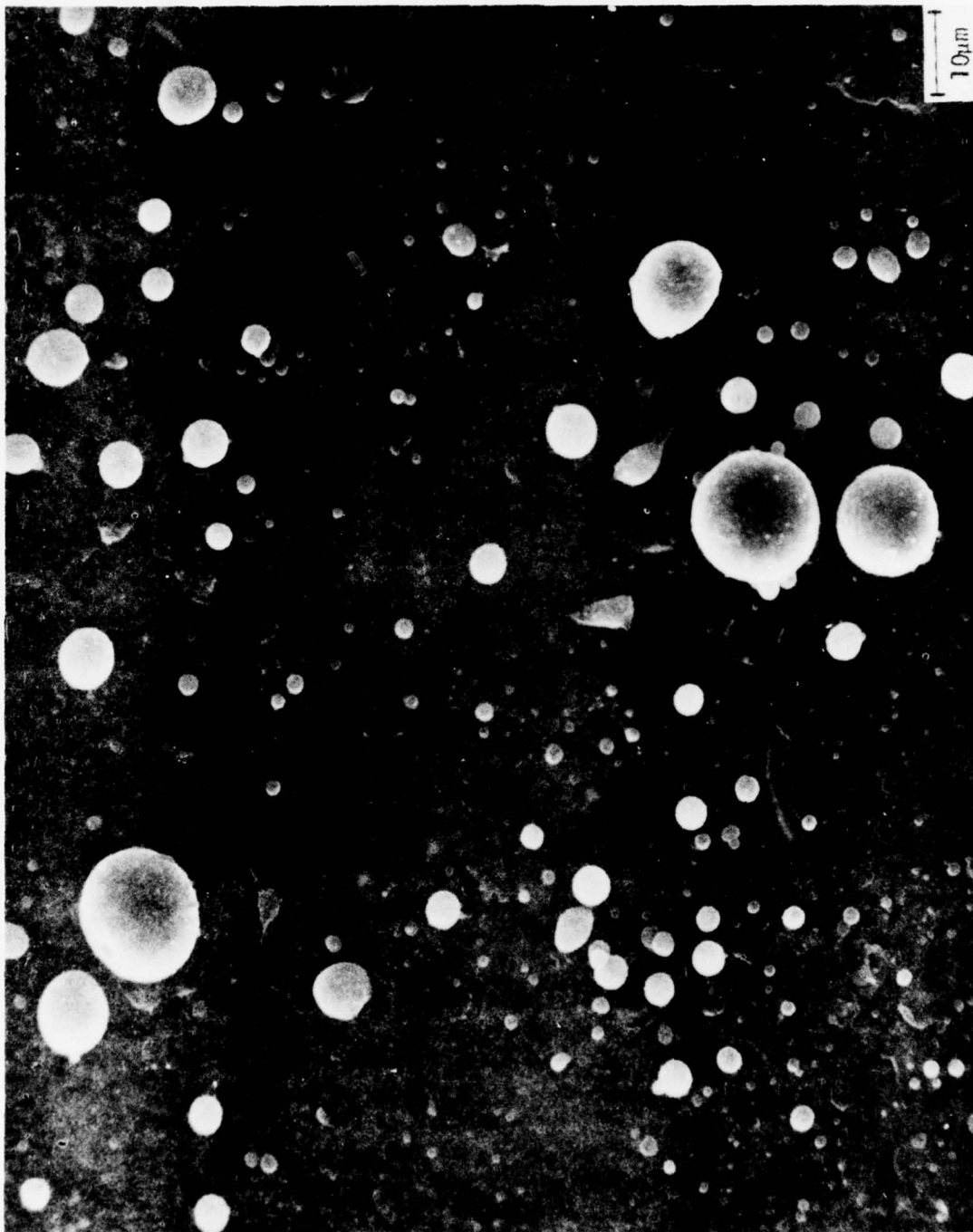
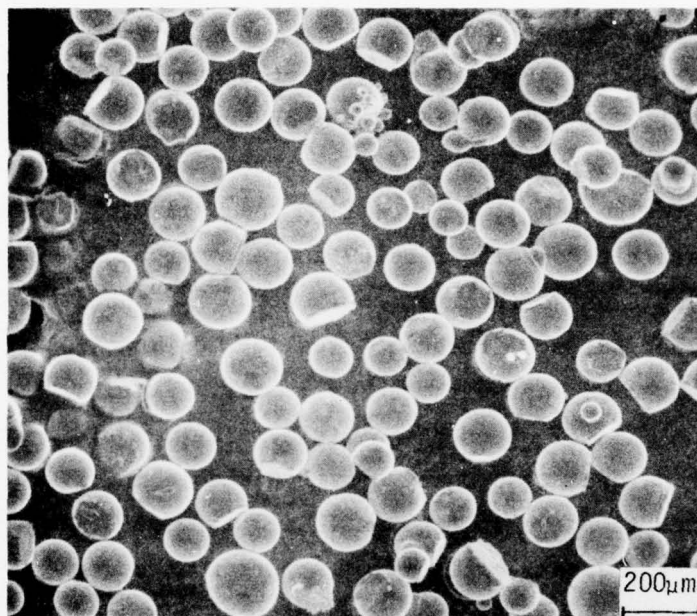


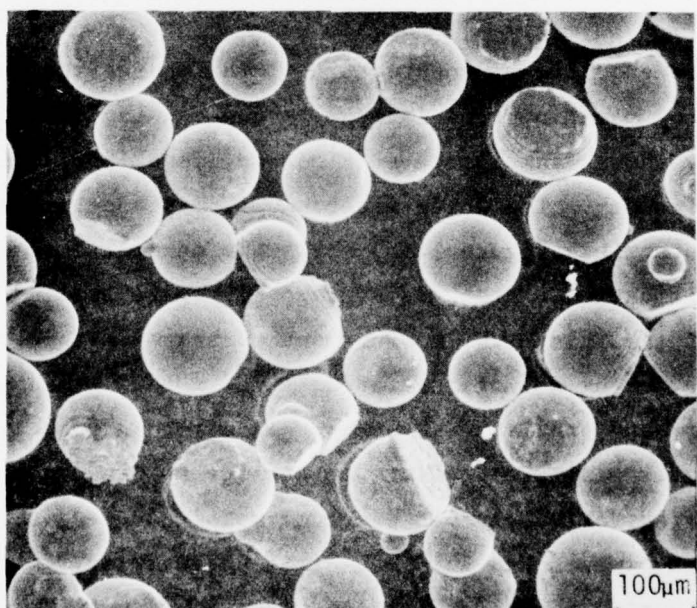
Figure 14. Secondary Electron Image of Fine Atomized Powders of Al-4.5% Cu Alloy Produced by the EHD Technique. The particles (less than  $0.2\text{ }\mu\text{m}$  to  $\sim 10\text{ }\mu\text{m}$ ) were rapidly solidified in flight. Collector (substrate) material was vinyl cellulose. Magnification, 2000X.

indicate that most of the coarse droplets generated at the source either partially solidified in flight or arrived at the collector as liquid. Figure 15 shows secondary electron images of the coarse powders, 100 to 150  $\mu\text{m}$  size range, removed from the collector. The partially flattened particles showing rippled surfaces probably contained low volume fractions of solid prior to impact. The spherical particles, with some minor surface irregularities due to impact, probably also solidified after contact with the collector. Figure 16 shows high magnification SEIs of one such particle. The dendritic structure of the particle surface is clearly distinguishable in figure 16(b). Similar structures to those in figures 15 and 16 were observed in particles removed from the copper collector. A larger percentage of these particles were partially flattened with rippled surfaces, indicating that they were completely liquid or only partially solid as they arrived at the collector.

The internal dendritic microstructure of the coarse atomized particles was studied by mounting them in epoxy and mechanical polishing. Figure 17(a) shows Back Scattered Electron Image (BSEI) of a representative coarse powder. The white interdendritic phase is the copper-rich  $\text{CuAl}_2 + \alpha$  eutectic. Figure 17(b) shows the dendritic structure at higher magnification. Measured average segregate spacing in this specimen is  $\sim 2 \mu\text{m}$ . This DAS measurement corresponds to a calculated cooling rate during solidification of  $\sim 2.2 \times 10^3 \text{ }^\circ\text{K/second}$  from Eq. (3). On the other hand, radiative heat flow calculations from Eq. (28) for a 100  $\mu\text{m}$  diameter particle predict an average cooling rate during solidification of approximately one order of magnitude less than that deduced from DAS measurements and Eq. (3). This observation, coupled with the directional nature of solidification noted in figure 17, verifies the hypothesis that solidification of these large droplets occurred after impact with the collector.

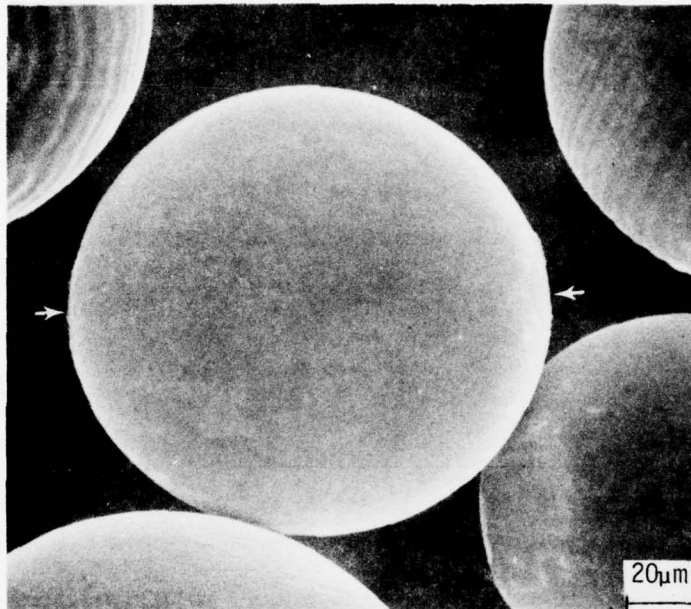


(a)

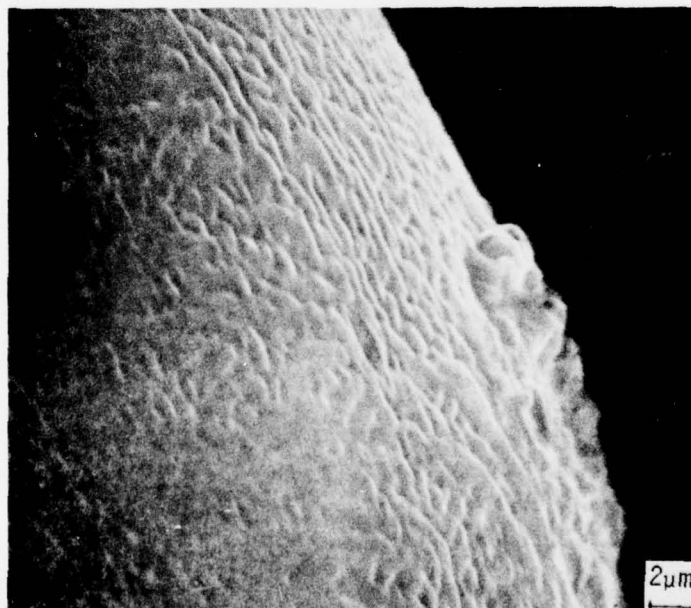


(b)

Figure 15. Scanning Electron Images of Coarse Atomized, 100 to 150  $\mu\text{m}$ , Powders of Al-4.5% Cu Alloy Produced in the EHD Apparatus. Powders were removed from the ground plate. The partially flattened particles showing rippled surfaces probably contained a low volume fraction of solid before impact. (a) 50X, (b) 100X.

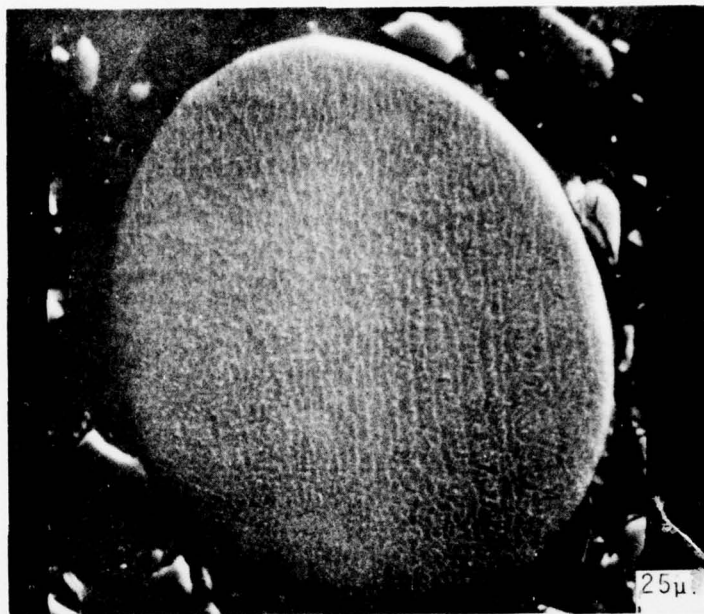


(a)

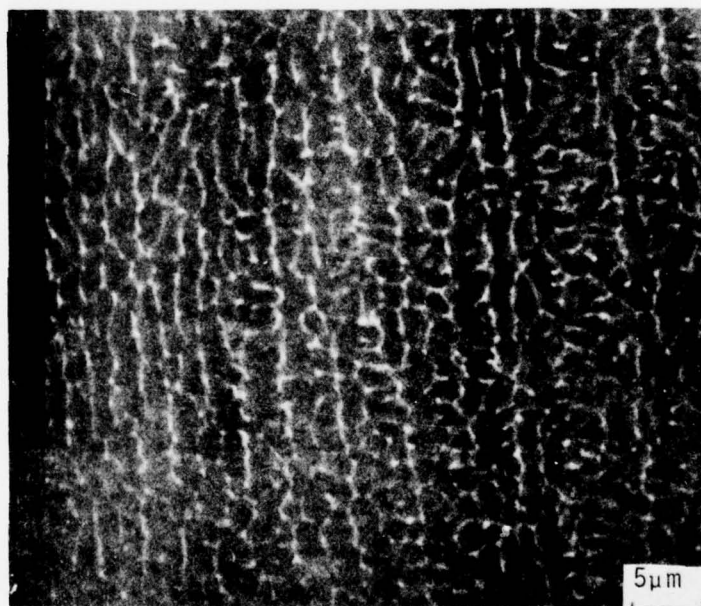


(b)

Figure 16. Scanning Electron Images of an Al-4.5% Cu Coarse Powder Almost Completely Solidified Before Impact. (a) 500X, (b) shows the dendritic surface structure at 5000X.



(a)



(b)

**Figure 17.** Backscattered Electron Images of the Internal Dendritic Structure of a Coarse Powder of Al-4.5% Cu Alloy Produced by the EHD Technique. (a) 800X, (b) 2000X.

Calculations presented in section 5 also show that radiative heat transfer is not a very effective method to achieve high cooling rates during solidification of low temperature alloys. On the other hand, high temperature alloy droplets, in the size range of  $1\text{ }\mu\text{m}$  or less should solidify at cooling rates in excess of  $10^5$  to  $10^6$   $^{\circ}\text{K}/\text{second}$ . Work is presently underway to investigate cooling rates in extremely fine droplets  $\sim 0.01\text{ }\mu\text{m}$  in diameter by radiative means only, as well as larger particles by combined convective and radiative cooling.

Work is also underway to:

- a. Develop the necessary techniques for careful control of process variables such that, at any given time during an experiment, a desired size range of droplets are produced
- b. Develop specific TEM specimen preparation techniques for the examination of the internal microstructure of the fine atomized (less than  $5\text{ }\mu\text{m}$  in diameter) powders

Finally, initial TEM studies indicate that the very fine (less than  $0.1\text{ }\mu\text{m}$  diameter) particles can be directly studied by this technique without any thinning of the powders. Preliminary TEM studies indicate that a substantial portion of the  $0.1\text{ }\mu\text{m}$ , or less, diameter particles are single crystalline.

## 6.2 SPLAT COOLING STUDIES

A second important capability of the EHD apparatus is its ability to produce controlled thickness, rapidly solidified splats of alloys on a variety of substrate materials. In these experiments, a substrate is simply inserted into the flight path of the fine atomized high velocity droplets generated at the source. A swivel arm retaining various substrate targets permits deposition and conductive cooling of the droplets for specified time periods. Splats of various thicknesses can thus be obtained, depending on the flow rate of the alloy through the source,

the fractional area of the jet covered by the target, and its residence time in the flight path. On impact, the high velocity of liquid droplets flatten out on the substrate. Successive impact of liquid droplets results in a rapidly solidified, splat cooled foil of the alloy. In the preliminary experiments performed during this contract period, three different substrate materials were employed for splat cooling of the Al-4.5% Cu alloy. These were thin,  $\sim 100\text{ }\mu\text{m}$  to  $500\text{ }\mu\text{m}$ , foils of vinyl cellulose, aluminum, and copper.

Figure 18 shows secondary electron images of a splat cooled Al-4.5% Cu alloy on a copper substrate viewed from the substrate surface. Figure 18(a) shows that the substrate was uniformly coated by the successively impinging liquid metal droplets. Higher magnification views, Figures 18(b) and 18(c), of the darker regions on the surface of the splat cooled specimen show individually splatted droplets with small spheroids emanating from their edges. While the individual splats are clearly distinguishable on the splat cooled surface, no such distinction could be made when the cross sections of the splats were examined. Figure 19 shows both top and edge views of a splat cooled specimen produced on an aluminum,  $100\text{ }\mu\text{m}$  thick foil, substrate. It is evident that successive droplets were welded together in a manner similar to classical splat cooled specimens - no layering effects were observed like those reported in the twin rolling experiments of Singer (Ref. 8). The relatively uniform ( $2$  to  $3\text{ }\mu\text{m}$  thick), featureless, cross sectional view of the splat in figure 19(b) shows that the EHD technique is an ideal method for preparation of rapidly solidified splat cooled specimens for subsequent fundamental studies via electron microscopy techniques. Absence of a distinguishable microstructure at magnifications of up to  $10,000\times$  in the splats produced to date indicates that either cooling rates were high enough to produce a complete solid solution of the alloy or that the substructure is so fine that it could not be observed at these magnifications. Work is presently underway to prepare appropriate specimens from these splats for TEM studies at higher magnifications.

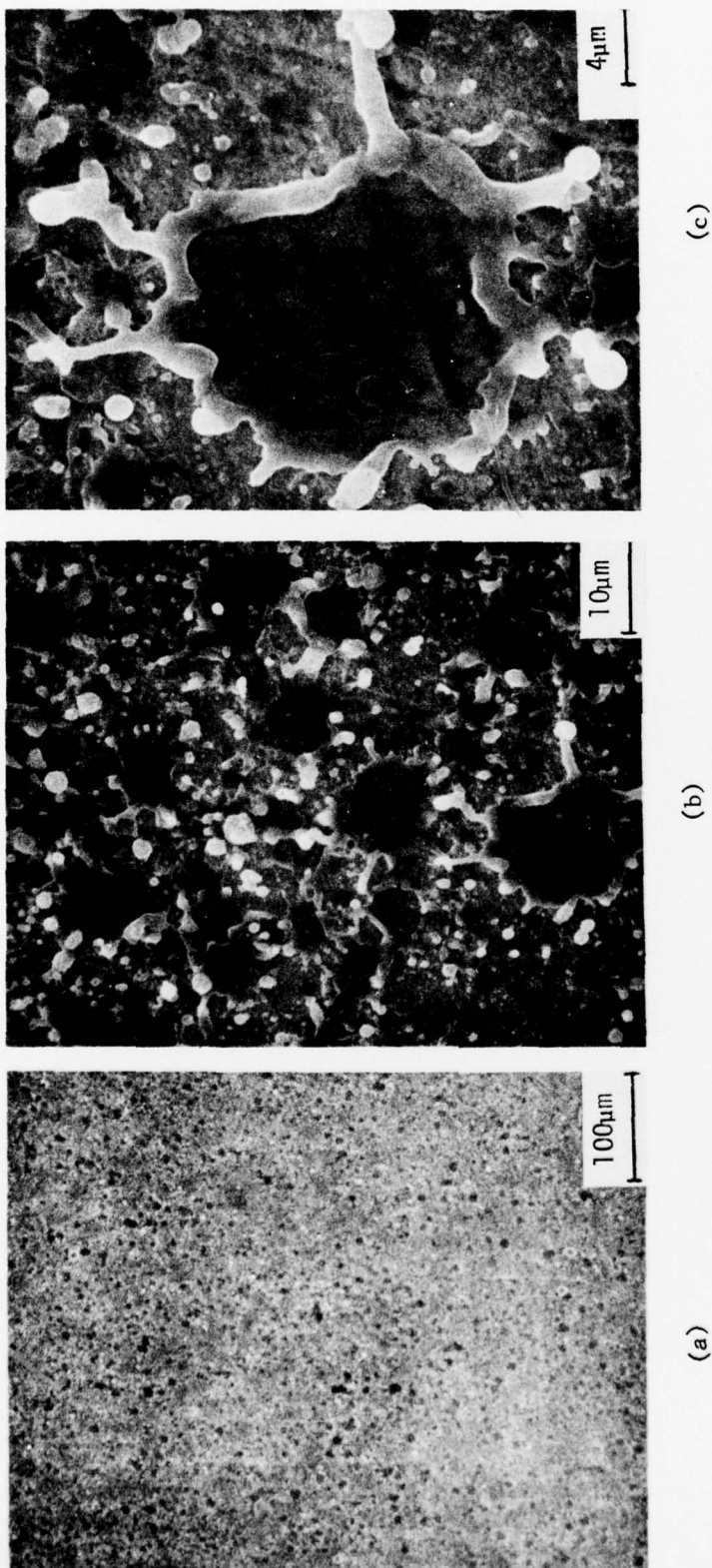
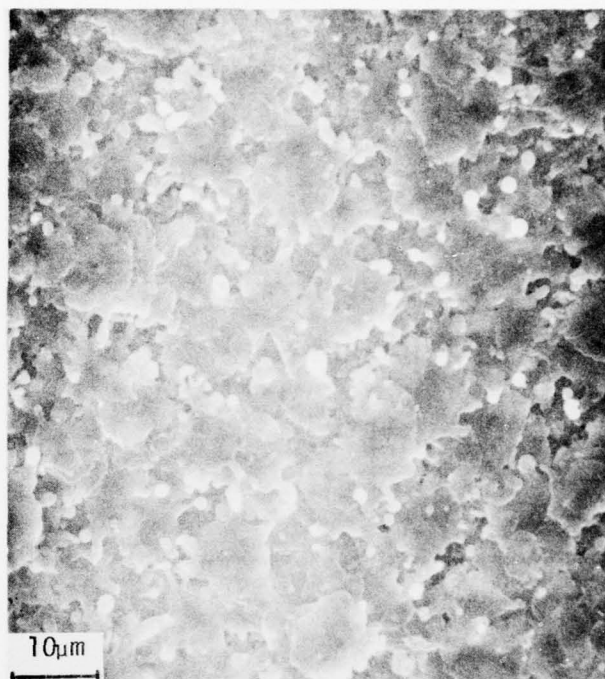
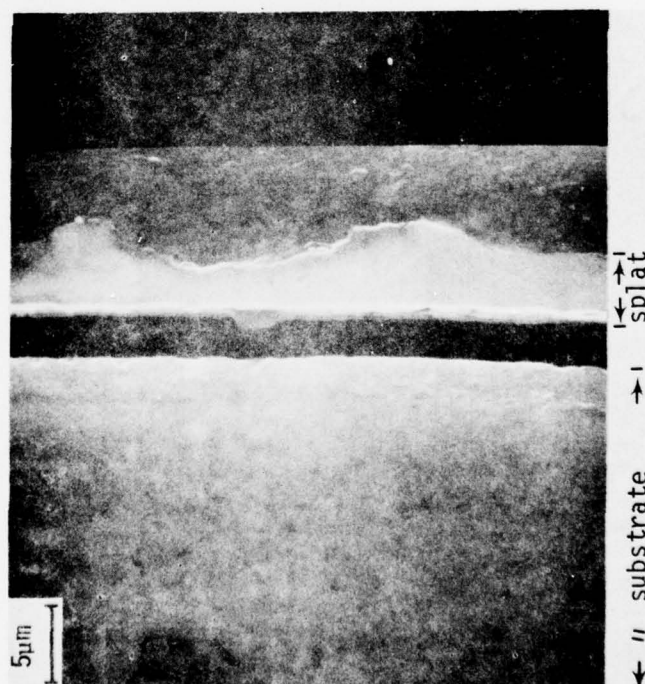


Figure 18. Secondary Electron Images of a Splat Cooled Specimen of Al-4.5% Cu Alloy Produced in the EHD Apparatus on a Copper Substrate. (a), (b), and (c) show views of the splat surface at 100X, 1000X, and 2500X, respectively.



(a)

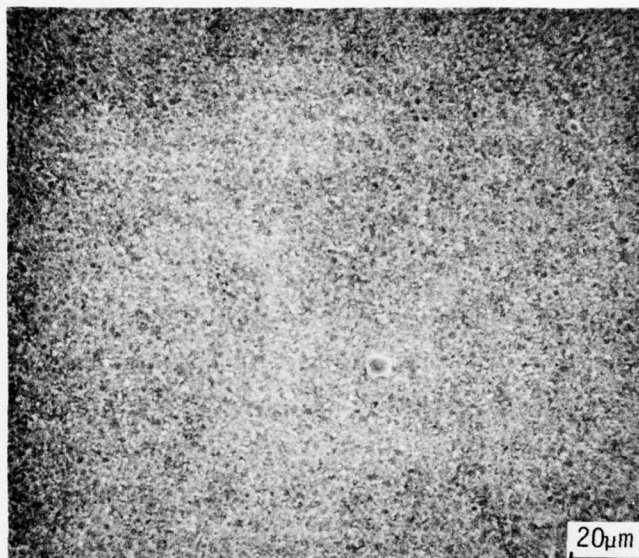


(b)

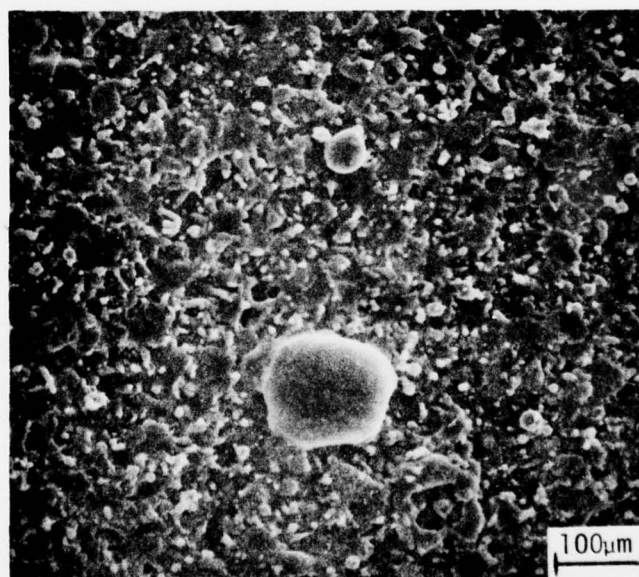
Figure 19. Secondary Electron Images of a Splat Cooled Specimen of Al-4.5% Cu Alloy Produced in the EHD Apparatus on an Aluminum Substrate. (a) shows a view of the splat surface at 1000X; (b) shows a cross sectional view of the splat and the substrate at 3000X.

The surface structure of a similar specimen produced on the vinyl cellulose substrate is shown in figure 20. The two large droplets protruding from the surface of the specimen are not unique to the vinyl cellulose substrate. Evidence to date indicates that liquid droplets spread less on this substrate than on the metallic ones.

As previously noted, a further aim of this study is to investigate the possibility of deposition of adherent thin films via the EHD technique. Figure 21 shows some evidence of welding between a splatted foil of Al-4.5% Cu alloy and an aluminum substrate. Work is continuing toward establishing the feasibility of producing adherent coatings by appropriate modification of the process variables, coupled with careful preparation of clean substrate surfaces.



(a)



(b)

Figure 20. Secondary Electron Images of a Splat Cooled Specimen of Al-4.5% Cu Alloy Produced in the EHD Apparatus on a Vinyl Cellulose Substrate. (a) and (b) show views of the splat surface at 100X and 500X, respectively.

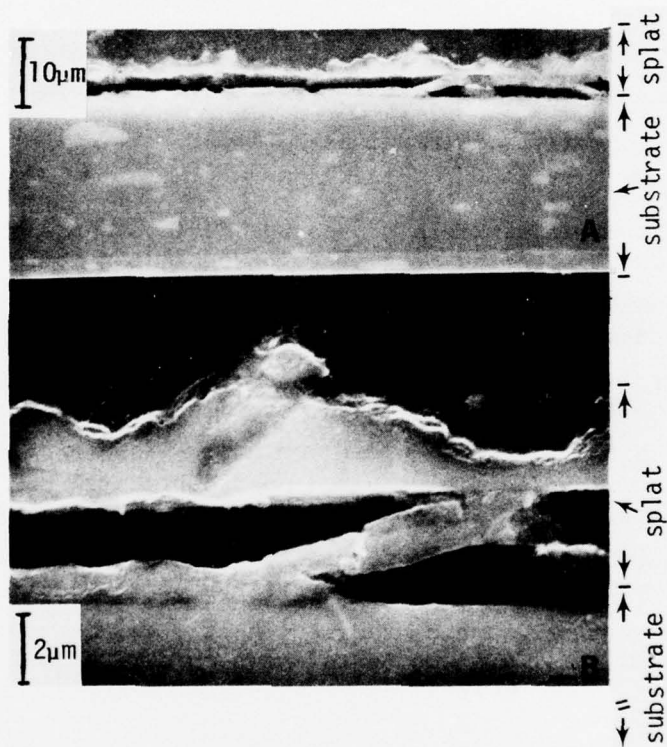


Figure 21. Cross Sectional View of an Al-4.5% Cu Alloy Splat Cooled Specimen Deposited on an Aluminum Substrate Showing Evidence of Welding Between the Two. Top and bottom secondary electron images are at 1000X and 5000X, respectively.

## SECTION 7

### CONCLUSIONS

This portion of the program has demonstrated the concept feasibility of a Table Top Amorphous/Microcrystalline Powder Generator using electrohydrodynamic methods. Accomplishments resulting from Phase I investigations are briefly summarized as follows:

- a. A ceramic particle source was developed and operated at  $1000^{\circ}\text{C}$  with the capability of extending performance to  $1300^{\circ}\text{C}$ .
- b. Submicron particles (less than 0.1 micron diameter) were generated using an Al-5.4% Cu alloy.
- c. Preliminary TEM analysis indicated that a large quantity of the submicron Al-4.5% Cu particles were single crystalline.
- d. Cooling rates of  $10^5$  to  $10^6$   $^{\circ}\text{C}/\text{second}$  were determined for submicron particles based on experimental evidence that particles solidified in flight before collection.
- e. Relatively uniform coatings (several micron thick) were deposited on various substrates using the Al-4.5% Cu alloy.
- f. Photomicrographic examination of a ceramic (alumina) nozzle used in Al-4.5% Cu tests shows no corrosive interaction.

The selection of the electrohydrodynamics approach for the production of amorphous substances, metastable phases, and materials showing increased solid solubility of solute elements is gaining in importance as an advanced materials processing technique. This work is complemented by the efforts of other investigators who recently demonstrated techniques for forming solid bars from metallic glass powder without destroying their useful properties. The advent of fabrication methods that will provide useful shapes to industry and research facilities, starting with powders, greatly enhances the possibility of the practical utilization of the EHD powder generation method.

## REFERENCES

1. H. A. Davies, Phys. Em. Glasses, 17, 159 (1976).
2. H. A. Davies, B. G. Lewis, Proceedings Second International Conference on Rapidly Quenched Metals, Edited by N. J. Grant and B. L. Giessen (1975), M.I.T. Press, Cambridge, Massachusetts, p. 259.
3. H. A. Davies, B. G. Lewis, and I. W. Donald, Proceedings on Rapid Solidification Processing: Principles, and Technologies, Reston, Virginia (November 1977).
4. R. Mehrabian, Proceedings of Conference on Rapid Solidification Processing: Principles, and Technologies, Reston, Virginia (November 1977), in press.
5. T. Z. Kattamis, W. F. Bower, R. Mehrabian, J. of Crystal Growth, 19, 229 (1973).
6. S. P. Iyer, W. V. Youdelis, J. of the Inst. of Metals, 101, 218 (1973).
7. T. Z. Kattamis, R. Mehrabian, J. of Materials Science, 9, 1040 (1974).
8. Proceedings Second International Conference on Rapidly Quenched Metals, Edited by N. J. Grant and B. L. Giessen (1975), M.I.T. Press, Cambridge, Massachusetts.
9. Proceedings of Conference on Rapid Solidification Processing: Principles, and Technologies, Reston, Virginia (November 1977) in press.
10. T. Z. Kattamis, R. Mehrabian, J. Vac. Sci. Tech., 11, 1118 (1974).
11. J. Perel, J. F. Mahoney, B. E. Kalensher, K. E. Vickets, and R. Mehrabian, Proceedings on Rapid Solidification Processing: Principles and Technologies, Reston, Virginia (November 1977) in press.
12. H. Jones, J. Phys. D.: Appl. Phys., 4, 1657 (1971).
13. L. Rayleigh, Phil Mag., 14, 184 (1882).